Synthetic Photometry of Hydrodynamic Simulations of Binary Star Systems

WHAT YOU SEE IS WHAT YOU GET: SYNTHETIC PHOTOMETRY OF HYDRODYNAMIC SIMULATIONS OF BINARY STAR SYSTEMS

By

KEVIN A. SOOLEY, B.SC.

A Thesis

Submitted to the School of Graduate Studies

in Partial Fulfilment of the Requirements

for the Degree

Master of Science

McMaster University

Master of Science (2014) McMaster University
(Department of Physics and Astronomy) Hamilton, Ontario

TITLE: What You See is What You Get: Synthetic Photometry of Hydrodynamic Simulations of Binary Star Systems

AUTHOR: Kevin Sooley, B.Sc.

SUPERVISOR: Dr. Alison Sills

NUMBER OF PAGES: xiv, 74

Abstract

In this thesis we present a procedure by which synthetic photometry of a hydrodynamic model of star or star-like object can be calculated in a regime where the photosphere is not radially resolved. In order to properly model the unresolved photosphere, we present a method where pressure and density are integrated outward from the outermost resolved radius of the star and then interpolated in temperature-surface gravity space between a set of MARCS (Gustafsson et al., 2008) stellar atmosphere models. These interpolations are accurate to within 10% of expected temperature values and are determined by minimizing the difference between the integrated pressure, density and surface gravity and that of the atmosphere model. Using the Monte Carlo Radiative Transfer code `radmc3d`(Dullemond, 2012), we produce blackbody spectra of stars and photometric light curves of equal and unequal mass detached binaries and a contact binary. Stellar blackbody spectra are accurate to better than 1%. Resultant light curves have less scatter than existing methods, such as `shellspec`(Budaj & Richards, 2004) and show the expected morphology. Our method allows for imaging directly from hydrodynamic simulations, with minimal user set-up. This procedure is designed with the intent of producing simulated photometry of stellar merger models.

Acknowledgements

First and foremost I would like to thank my supervisor, Dr. Alison Sills. Without her continued, unwavering support and helpful advice, this thesis would never have been completed. It is difficult to adequately express my gratitude for her help. I would also like to thank my committee members individually, Dr. James Wadsley for his helpful and informative course on Radiative Transfer, upon which some results in chapter three are based, and Dr. Doug Welch, for helping me step back and think about the goal of this thesis in a broader context. Without these three individuals, this work could never have been completed.

I'd also like to thank the main support structure in the department, my friends. In particular, Ben Keller for reintroducing me to bicycles, without which I am certain I would never have finished this project with my sanity intact. I'd like to thank the Liquid State softball team, including Rachel Ward-Maxwell, Tara Parkin, Jonathan Newton, Damien Robertson, Sam Benincasa, Alyssa Cobb, Corey Howard and Aaron Maxwell for attendance and coffees, and Alex Cridland, Damien Robertson and Kaz Sliwa for sharing in the misery that is pitching. I would also like to thank Matt McCreadie for always keeping his promises and for L.P. Hovercraft.

My parents have been always supported me, and I must thank them deeply for the financial assistance and emotional support over these few months in particular.

Finally, my wonderful partner Kayla has supported me throughout these last two years, and it is this support for which I am most grateful.

As always, to Sarah and Zach Rose

Table of Contents

List of Figures

List of Tables

Chapter 1

Introduction

Most[1] stars appear as single, unresolved points of light in nearly all observations. The details of their structure and evolution are revealed to us through careful study of their emitted light. Spectroscopy, the analysis of light emitted at different wavelengths, can reveal composition as well as many other properties, and can be used to probe the surface of a star which is thousands of light years away (*e.g.,* see Abazajian et al. (2009)). Spectroscopy is expensive and time-consuming, requires a signal to noise ratio of 100 or higher to obtain certainty within 1%, as well as a high resolving power R. R is defined as $\frac{\lambda}{\delta\lambda}$ where λ is the observing wavelength and $\delta\lambda$ is the smallest wavelength difference the instrument can distinguish. A less time-intensive, but less detailed method is called photometry. Photometry simply collects photons in a well-defined wavelength range, called a bandpass, and is less time consuming than spectroscopy. These bandpasses are also called Photometric colours. Photometric colours can be used to compare the total flux emitted in different portions of the electromagnetic spectrum. Since stars mostly emit light like classical blackbodies, they will be inherently brighter in certain regions of

---

[1] The notable exclusion is *the Sun*

the electromagnetic spectrum according to a function that depends mainly on their surface temperature. However, stars are only *approximately* blackbodies.

Photometry and spectroscopy have numerous applications in astronomy from probing the interior of stars via astroseismology (Gilliland et al., 2010), to exploring the expansion of the universe (Riess et al., 1998; Spergel et al., 2003). These methods reveal that a considerable fraction, and even a majority are in fact, multiple systems. Around 50% (Duquennoy & Mayor, 1991; Raghavan et al., 2010) of stars that we see in the sky are not actually single stars, but multiple systems of two, three, four or even more stars which are all bound gravitationally.

The simplest way to determine if a star is single or not is to observe it photometrically, over a long period of time. However, this observation will vastly underestimate the number of binary systems, as it will only detect systems with orbital planes perpendicular to the plane of the sky. Binary stars orbit one another with a well defined period which comes from Newton's version of Kepler's Third Law

$$P^2 = \frac{4\pi^2}{G(M_1 + M_2)} a^3. \tag{1.1}$$

Here P is the period of the orbit of two stars with masses M_1 and M_2 with a semi-major axis a and G is Newton's constant of universal gravitation 6.67384×10^{-11} m^3 kg^{-1} s^{-2}. Kepler's first law tells us that celestial orbits take the form of ellipses. The semi-major axis is the analogue to the radius of a circle, but when measured on the longest axis of the ellipse. If the axis of the orbit is approximately perpendicular to the plane of the sky, the stars will undergo mutual eclipses, and so long-term monitoring of the orbit will produce a light curve with periodic dips, which reveal the physical size and effective temperature of the stars. Unfortunately, this method is limited because eclipses are *required*, so only a small fraction of the inclination parameter space is amenable to binary detections via photometric detection.

A more general method is based on spectroscopic techniques. Since stars are not perfect blackbodies, but instead have spectral lines, and considering that binary stars orbit a common centre of mass, we can observe Doppler shifts as the stars move towards or away from us. This motion will, in general, have a radial and a tangential component, unless the plane of the orbit is parallel to the plane of the sky. In all other cases, the spectral lines of the stars will be shifted, with the shift depending on the radial velocity, which is a periodic function of the orbital phase. A radial velocity measurement produces a signal much like the one shown in Figure 1.1 where the semi-amplitude K is given by

$$K_1 = \left(\frac{2\pi G}{P}\right)^{\frac{1}{3}} q M^{\frac{1}{3}} \frac{sini}{\sqrt{1-e^2}} \tag{1.2}$$

which is the radial velocity equation. Here M is the total mass of the binary system, q is the mass ratio $\frac{M_1}{M_2}$, P is the orbital period and i and e are the orbital inclination and eccentricity, respectively. In addition to this signal, since the radial velocity method is inherently spectroscopic, we also have access to all the stellar attributes normally obtained via spectroscopy, in particular surface gravity and effective temperature, of one or both of the companions, depending on the mass ratio q. In the case of approximately equal-mass systems with comparable luminosities, two sets of spectral lines may be visible.

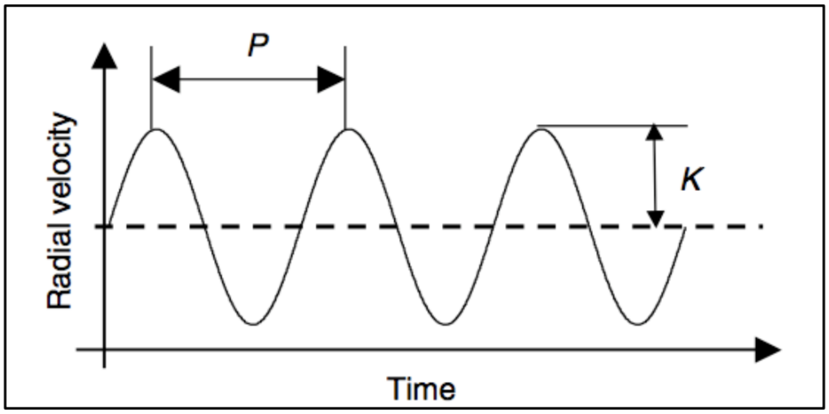

[htb]

Figure 1.1: An illustration of how the period P and semi-amplitude K can be determined from radial velocity data. Image Credit: Planetary Systems and the Origins of Life, Cambridge University Press, 2007

With the results from photometric and spectroscopic surveys of the sky, we can determine some statistics and trends of binary stars. Raghavan et al. (2010) reports, for stars like the sun:

1. More massive stars have a larger tendency to be binary.
2. The orbital period distribution follows a roughly Gaussian distribution with a peak at P$\simeq$ 293 years and a standard deviation $\sigma_P \simeq 190$ days.
3. The period-eccentricity distribution shows that orbits are circularized over the age of the galaxy for periods less than 12 days. For larger periods, the distribution is roughly flat.
4. The mass ratio distribution shows a preference for equal mass pairs, particularly in systems with small orbital periods.

While the majority of binary systems have large periods, in the realm of many years and even several centuries, there is a small population with periods of a handful of days and smaller. Through equation 1.1 we can see that these systems have very small semi-major axes, making the components of these systems are so close to one another that differential tidal forces become increasingly important. Because of this, as the orbital periods become very short, around 3 days or less, the stars can actually begin to distort from their ordinary spherical states into a "tear drop" shape, given by the Roche potential (see Kopal (1959)). If the periods get shorter still, the tear drop shapes can actually make contact with one another, and the two stars become one extended object *in hydrostatic equilibrium.* The physics governing *contact binary* formation and subsequent evolution is poorly understood, making these objects rich for further study. One thing, however, is certain: the end state of their evolution is a merger event (Gazeas & Stepien, 2008).

Merger events are rare, and until recently, none had been observed. This all changed with the outburst of V1309 Scorpii in 2008. Nova Scorpii (Sco) 2008 was reported by Nakano et al. (2008) as a 9.5-10 magnitude outburst with two previous non-detections at limiting I band magnitudes of 12.8 and 12 on the 20th and 21st of August 2008. Outbursts of this type are called red novae, which is a type of stellar explosion. Spectra were taken September 3rd, 4th and 5th, revealing a nova with a few emission lines, but mostly narrow absorption lines which did not return to its initial brightness for a considerable time, nearly a year, after the outburst. Near-infrared spectroscopy revealed a cool (M type) giant with molecular absorption bands due to from CO and H_2O, with some TiO and VO. Luckily, this object happened to lie in the monitoring fields of the Optical Gravitational Lensing Experiment (OGLE) project. OGLE had been collecting data on V1309 Sco continuously with over 2000 observations in the Cousins I band, centred at 786.5 nm with a width of approximately 100 nm. Observations began in August 2001 and excluding periodic conjunctions with the sun, continued until late 2010 (Tylenda et al., 2010). Upon analysis of the photometry, a light curve, shown in Figure 1, revealed that this outburst was in fact the result of a binary merger of a contact binary. The scatter of approximately 0.5 magnitudes in the light curve before the outburst is strictly periodic with a period of 1.4 days. The period decreased exponentially, with a least squares fit for the period given by

$$P = 1.4456 exp\left(\frac{15.29}{t - t_0}\right) \tag{1.3}$$

where P is the period in days, and t is the observation date and t_0 is the Julian Date 2 455 233.5. Recent simulations by Nandez et al. (2013) reveals a likely progenitor comprised of a 1.52 $M_\odot$ giant primary and a 0.16 $M_\odot$ companion. The companion was either a main sequence star or the stripped core of a giant, with either producing a V1309 Sco type analogue. However, the best case progenitor is a synchronised binary with a main sequence companion.

The task of modelling a contact binary system from Zero Age Main Sequence through contact to merger is non-trivial because of the vast ranges in time scales of the phenomena involved. For example, the orbital period evolves over megayears, while the orbital period itself is no more than a few days (Gazeas & Stepien, 2008; Tylenda et al., 2010; Stepien, 2011). In order to produce synthetic photometry events such as the V1309 Sco merger, this modelling must be done precisely, and also requires an understanding of how the object would appear to a distant observer. This thesis tackles a single aspect of this modelling, namely determining how to accurately produce simulated

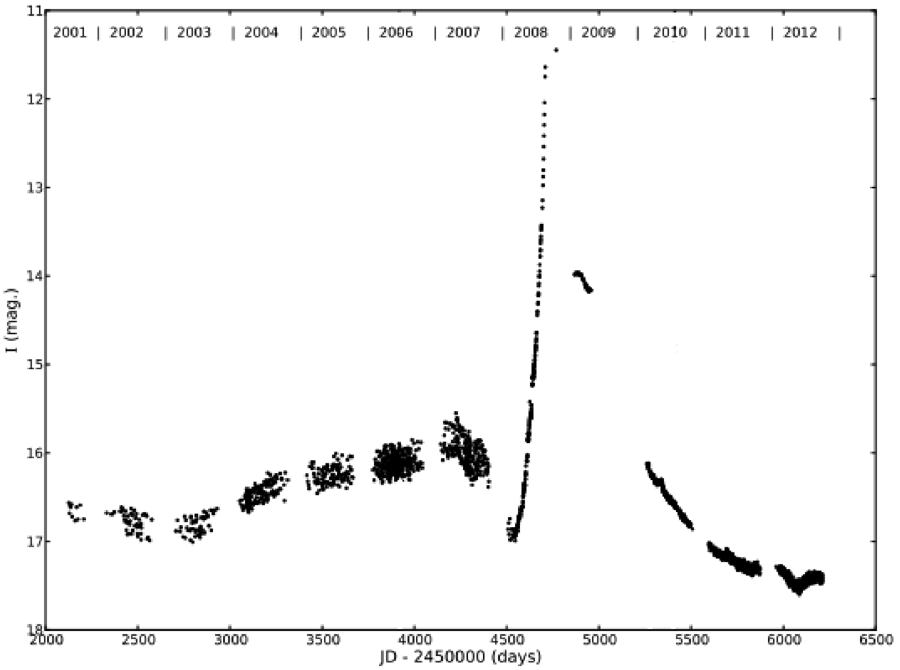

Figure 1.2: I magnitude of V1309 Sco as a function of time, from OGLE III and VI. Reprinted with permission from (Tylenda et al., 2010)

photometry of a hydrodynamic model of a contact binary as it evolves through contact. Previous work in the field focused on modelling photometry and spectroscopy of static systems such as binary stars or quasi-static systems such as binary stars with disks, jets and spots. For more information, the reader is referred to Budaj & Richards (2004) and the references located in their introduction. Raw imaging of purely hydrodynamic simulations is currently a hot topic in the field of radiative transfer, with several codes in development for various aspects of the problem (See Stamatellos & Whitworth (2005),Forgan & Rice (2010) and Robitaille (2011)). However, these codes have a distinct tendency to focus on structures larger than the scale of binary stars (e.g, star forming regions to quasars) where there is a considerable amount of optically-thin material. Such simulations tend to concern themselves mainly with the interaction of light and astronomical dust, whose interactions are considerably simpler than that of light and gas. The difficulty in radiative transfer in the stellar regime comes from the vast range of the state variables such a temperature, pressure and density. To circumvent this difficulty, we take advantage of the fact that each star is optically-thin in a very small radial region and is in thermodynamic equilibrium inside of that region. The second chapter of this thesis will explore the relevant theory behind the methods used to determine both the intensity of light leaving the surface and the star and the details of this outer region of the star, called the atmosphere, where this light escapes using physically motivated, reliable models of stellar atmospheres. These methods are then applied to several test systems to determine their validity in this unusual regime. These test systems are simple and hierarchical, with the success of each test depending on the results of the previous one. The success of these tests indicates that this method is likely applicable for use in producing simulated photometry of dynamically evolving systems in this regime. Future work, conclusions, caveats and cautionary tales for the future of this project will be outlined and discussed in Chapter 4.

Chapter 2

Methods

In this chapter I will describe the main methods used in the course of this thesis. There are two separate parts which must work together in order to obtain simulated photometry from hydrodynamic models of stellar mergers. Firstly, we have to be able to understand where the fluid in the stars go as they merge. This can be accomplished by hydrodynamic modelling. While the hydrodynamics tell us where the fluid is, it gives us no direct information about the light emitted by the object. In order to make synthetic images and photometry, a radiative transfer algorithm must be employed. Radiative transfer comprises a set of tools to model how light travels interacts with matter as it travels through it. Monte Carlo radiative transfer has been chosen for this purpose, and will be outlined in the first section of this chapter. As an input, any radiative transfer scheme will require density, temperature and opacity information. The density and temperature are primarily determined by the hydrodynamic modelling, and we require a source of relevant opacities. I will outline the model stellar atmospheres used to determine these opacities in the second section of this chapter.

In order to produce hydrodynamic models, an algorithm for solving the equations of hydrodynamics, for example Smoothed Particle Hydrodynamics (SPH), can be employed. SPH was developed independently by Gingold & Monaghan (1977) and Lucy (1977). In SPH, the fluid is replaced with a set of particles, each assigned a density, pressure and internal energy. To retain the continuum properties of fluid mechanics, the particles are smoothed over a finite distance, to allow for the calculation of a continuous pressure and density from a discrete set of particles. These *smoothing lengths* are large enough that they the sphere of influence of a particle overlaps with a number of its neighbours. SPH can be constructed in such a way that it inherently conserves energy, which makes it a valuable tool in modelling binary stars, as we require the orbital energy to be stable over a large number of orbits. Reviews of the key algorithms and astrophysical applications can be found in Springel (2010) and Price (2012).

2.1 Monte Carlo Radiative Transfer

Smoothed particle hydrodynamics codes tell us where the mass of the fluid is, but to compare with astrophysical observations we need to know where the light is coming from. This requires the use of a radiative transfer algorithm, of which there are two main classes. The Flux-Limited Diffusion algorithms are mainly effective in optically-thick regions, where the radiation propagation can be treated as a diffusive process (See Boss (2008) for a more detailed description). This is an efficient method for determining the radiation field in the interior of an optically-thick object, but fails as the object becomes optically-thin. In optically-thin regions, a scheme called Monte Carlo Ray Tracing (MCRT) is more efficient, as the modelled photons will only undergo $\sim$1 interaction before escaping from the medium. For our purposes we will use the MCRT radiative transfer algorithm, via the `radmc3d` code, which is based on a ray tracing method, where rays are cast along grid cells, with the length of these rays being randomly distributed (see Dullemond (2012) for details). Section 2.1.1 will discuss the operation of this code in more detail. This choice is motivated by the fact that the entirety of the information which we receive from a star is emitted in a small, optically-thin, radial region called the photosphere, which will be discussed in the second section of this chapter.

In MCRT photons are created, travel some distance, and something happens to them (either scattering or absorption). This process repeats until either the photon is determined to be trapped forever or escapes from the medium. Artificial images are created in much the same way a real image is created on a CCD chip in a telescope. To take an image, we need to define an image plane at some angle and location relative to the source we're attempting to image. This image plane is divided into pixels, and only photons whose trajectories *after escaping the medium* cross the image plane will be counted in the image.

To talk more about this, we'll need to introduce concepts from radiation transfer, namely intensities, cross sections, optical depths and fluxes.

2.1.1 Basic Machinery The photons carry a total energy E_ν which is split equally among them, so each packet carries energy dE_ν. The photons also have a direction of travel and are related to the specific intensity I_ν, defined as the radiant energy dE_ν crossing a surface area dA at an angle θ to the surface normal within a solid angle $d\Omega$ in a frequency range $d\nu$ in time dt, or, more succinctly following Rybicki & Lightman (1986),

$$I_\nu = \frac{dE_\nu}{\cos\theta \; dA \; dt \; d\nu \; d\Omega} \tag{2.1}$$

which has units of ergs cm^{-2} s^{-1} Hz^{-1} sr^{-1}. Flux, defined as

$$F_\nu = \int I_\nu \; \cos \; \theta \; d\Omega \tag{2.2}$$

is the rate of energy flow across an area dA per unit time per unit frequency with units ergs cm^{-2} s^{-1} Hz^{-1}. Photon interactions are inherently probabilistic, with interactions determined by scattering and absorption cross sections. Cross sections, σ are related to the difference between incoming and outgoing energies at a point, and are defined by the energy removed from the system per second per frequency per solid angle, so

$$\Delta E_{t,\nu} = I_\nu \sigma \tag{2.3}$$

where $\Delta E_{t,\nu}$ is the energy removed per second per frequency.

The equation of radiative transfer is

$$\frac{dI_\nu}{d\ell} = -I_\nu \kappa_\nu + j_\nu \tag{2.4}$$

where κ_ν and j_ν are the opacity and emissivity of the medium respectively. If we define the optical depth τ_ν along a line of sight L as

$$\tau_\nu = \int_L \rho \kappa_\nu dx \tag{2.5}$$

we can rewrite equation 2.4 as

$$\frac{dI_\nu}{d\tau_\nu} = -I_\nu + S_\nu \tag{2.6}$$

where $S_\nu = j_\nu/\kappa_\nu$ is called the source function of the medium. Note that the opacity κ is related to the cross section σ by the following

$$n\sigma = \rho\kappa \tag{2.7}$$

where ρ is the mass density of scatterers and n in the number density of scatterers.

2.1.2 Interactions: Scattering and Absorption

A photon travelling through a medium can either be scattered or absorbed and the probability of the former depends on the albedo, a, defined as

$$a = \frac{n_s\sigma_s}{n_s\sigma_s + n_a\sigma_a} \tag{2.8}$$

where n_s and n_a are the number densities of scatterers and absorbers with interaction cross sections σ_s and σ_a respectively.

We can define the mean free path of a photon as

$$\ell = \frac{1}{\rho\kappa}. \tag{2.9}$$

And so, following Peraiah (2002), the probability of an interaction within an infinitesimal length $d\ell$ is

$$\frac{d\ell}{\ell} = \rho\kappa d\ell \tag{2.10}$$

and the probability of no interaction follows;

$$1 - \frac{d\ell}{\ell} = 1 - \rho\kappa d\ell. \tag{2.11}$$

By defining a distance x as N segments of length dx, we can write the probability of no interaction as

$$P(x) = \left(1 - \frac{\rho\kappa x}{N}\right) \cdot \left(1 - \frac{\rho\kappa x}{N}\right) \cdots = \left(1 - \frac{\rho\kappa x}{N}\right)^N \tag{2.12}$$

which for large N can be rewritten as

$$P(x) = 1 - \rho\kappa x = e^{-\tau} \tag{2.13}$$

where τ is the optical depth[1] and we have taken advantage of the Taylor expansion of e^x. So the complementary probability that an interaction does occur is simply

$$P(\tau) = 1 - e^{-\tau}. \tag{2.14}$$

From this distribution we sample τ, or equivalently L, the distance a photon travels between interactions, such that

$$\tau = -log(1 - \xi) \tag{2.15}$$

where $\xi \in [0, 1]$ is a uniformly distributed random number. An interaction is a photon absorption or scattering event, where the photon's direction of

---

[1] Note that the optical depth is just the number of photon mean free paths between the source and the surface.(Carroll & Ostlie, 2006)

travel changes. Assuming isotropic scattering, the distribution of scattering angles is

$$P(\mu, \phi) d\mu d\phi = \frac{d\mu}{2} \frac{d\phi}{2\pi} \tag{2.16}$$

where we sample random numbers $\xi_i \in [0, 1]$ such that

$$\mu = 2\xi_1 - 1 \phi = 2\pi\xi_2 \tag{2.17}$$

where μ and ϕ are the new angles of travel. Equation 2.15 is then sampled for a new distance of travel. If the photon escapes the fluid, it is propagated onwards until it is collected on an image plane. If not, Equation 2.17 is sampled again, the photon is scattered or absorbed and the process repeats until it escapes.

The Monte Carlo aspect of Monte Carlo radiative transfer comes in to play when this process is iterated multiple times, generally in order to conduct a temperature calculation. In this case, photons are emitted and, when absorbed, they deposit energy into their absorbing cells. This process is then repeated until an equilibrium temperature is attained. However, this temperature correction process is remarkably slow in a stellar regime, where cells are very optically-thick, with optical depths much larger than 100. Since this method is incredibly inefficient, we will take advantage of stellar atmosphere models to more accurately determine surface temperatures. More details on this determination can be found in Chapter 3.

2.2 Stellar Atmospheres

A defining moment of undergraduate education in astronomy is the discovery and understanding of the simplicity of the equations of stellar structure. Probing the internal structure of a star with these equations, representing hydrostatic equilibrium, conservation of mass and an model of energy generation is a beautiful exercise showing the power of simple models in understand complex systems. The bulk of a star in well modelled by these questions, and it is these equations can be solved numerically to determine the bulk interior structure of stars of varying masses and evolutionary states. In this interior region the density ρ, pressure P and temperature T vary smoothly and energy transfer is dominated either by convection or radiation, depending on the temperature of the region. These equations can be solved numerically, to yield full profiles of P, ρ and T from the centre to virtually the surface.

However, this model is not adequately detailed. The outer layer of the sun, called the photosphere, is a region where the star transitions from the optically-thick regime to the optically-thin regime and the temperature drops dramatically. For example, for the M=0.7 $M_\odot$ model from YREC, this drop occurs over a range of about 500 km (approximately 0.07% the stellar radius). The temperature drops by approximately two orders of magnitude in this range, and it is this region which sets the spectrum which we detect in our telescopes. While this is a small region in both mass and radius, pressure has a relatively large range, varying by several orders of magnitude.

Because this region varies from “mildly” optically-thick ($\tau >$100, which is enormously thick in most cases but optical depths in stars can easily reach

10^6) to extremely optically-thin ($\tau \sim 10^{-5}$) (Gustafsson et al., 2008) a proper understanding of the photosphere requires detailed calculations of atomic transitions (see Kurucz (1995)), opacities (see Seaton et al. (1994)) and chemical abundances as it is here that all detectable spectral lines are produced, and the relatively homogeneous radiation field from the interior of the star is "fingerprinted" by the atmosphere. Understanding this region is further muddied by the loose terminology. Model atmospheres are actually model *photospheres*, and in the photosphere hydrostatic equilibrium is reduced to

$$\frac{dP}{d\tau} = \frac{g}{\kappa_\nu}. \tag{2.18}$$

In the interior of the star, it makes sense for the equations of stellar structure to the written in terms of mass or radius, as those quantities change rather dramatically. However, in the atmosphere, the enclosed mass is essentially constant, and the radius changes by no more than a tenth of a percent. Because of this, the only quantities that matter are $g = GM/r^2$ and opacity. All the complex physics of atoms and molecules in the outer layers of the star is taken in to account in the calculation of the opacity, and accuracy here is crucial, as it is this region from which *all of the light from the star* escapes.

Opacities are dependent on a number of factors. Opacity κ_ν measures the amount of light attenuated from a source per unit mass of material between the observer and the source. Opacities in low mass main sequence stars are due mainly to hydrogen scattering and metal lines (Gustafsson et al., 2008, and references therein). Spectral lines are formed by bound-bound transitions which are electronic transitions within an atom, when an electron jumps from one level to another, absorbing or emitting a photon. The continuum opacity is produced mainly by hydrogen is due to two different processes. A Bound-free transition or photoionization is the complete removal of an electron from an atom by an incident photon. Free-free absorption is a transition which occurs when a charged particle scatters off a another nearby charged particle and absorbs a photon in order to conserve energy and momentum. Finally, electrons can scatter off one another producing a wavelength independent opacity which dominates in high temperatures regions. Spectral lines are not usually included in the determination of κ_ν, with the notable exception of an effect called line-blanketing (Gustafsson et al., 2008). The wavelength dependent opacities are continuous and do not contain lines *per se*, becase to include all atomic lines would be an incredible challenge, considering the sheer number of transitions from heavier elements. These transitions are also often very close to one another, such that their wavelength ranges overlap and turn lines into bands. This is line-blanketing, which causes a large number of *line opacities* to appear as a *continuous opacity*. So, taking advantage of this, the MARCS atmospheres *sample* these opacities at regularly-spaced points in frequency space to determine an approximate wavelength continuum opacity, as described by Peytremann (1974) and Sneden et al. (1976). Each of these pieces constitutes an entire field on its own, and so an accurate atmospheric model for a star is an machine with many, many parts. Moreover, a detailed understanding of the atmosphere region of a star is crucial to understanding the spectrum from a star. The transition from optically-thin to optically-thick occurs in this region, and the surface of a star is defined as the region where $\tau = \frac{2}{3}$, or a photon has $e^{-2/3}$ or about 50% chance of escaping.

One particular brand of model atmospheres is the Model Atmospheres in Radiative and Convective Scheme or MARCS (Gustafsson et al., 2008). MARCS atmospheres provide the user with a grid of models with temperatures from 2500 to 8000 K, surface gravities between $10^{3.5}$ and 10^{5} in cgs units and [Fe/H] ranging from 10^{-5} to 10^{1}. There are a total of 52,000 models available, spanning the range of solar type stars with varying chemical abundances. Each atmosphere consists of wavelength dependent opacities, approximate surface fluxes and chemical abundance information (http://marcs.astro.uu.se/index.php). Because the MARCS atmospheres include information about chemical abundances, individual lines can be added on top of the continuum opacity, if the user is interested in spectral calculations. For our purposes, and as a first step, a continuum opacity is adequate. Any method that works with an continuum opacity can easily be extended to include spectral lines.

A radiative transfer algorithm coupled with a physically-motivated model for a wavelength dependent opacity are all we need to image hydrodynamic simulations. The following chapter will outline a set of simple sanity checks to examine the validity of this proposed method, as well as a method to determine surface temperature *a priori* from the internal structure of the star.

Chapter 3

Synthetic Photometry Workflow

In this chapter I will present the steps required to take an SPH simulation of a stellar system and, using the Monte Carlo Radiative Transfer tool `radmc3d`, produce either synthetic images or synthetic black-body spectra. With the stellar atmosphere models from MARCS and the SPH stars from YREC, there is still a piece missing. Because the stellar atmosphere models are ~ 500 km thick, the SPH stars cannot perfectly resolve the YREC stars. In order for the SPH particles to behave like a fluid, each particle's smoothing length must overlap with the position of a user-defined number of nearby particles. To achieve a smoothing length of less than 500 km in a star of radius 1 $R_\odot$ would require hundreds of millions of particles, which is not computationally tractable at this time. This limit causes the atmosphere to be unresolved, in addition to a small radial region between the atmosphere and the SPH star where mass is essentially constant, but pressure decreases dramatically with density. It is the modelling of this region that will be outlined and justified in the following sections.

Firstly, SPH simulations must be set up and evolved. Our SPH stars are built up from YREC radial profiles of pressure and density. Each particle is initially assigned the same smoothing length h. In order to bring the sphere of SPH fluid to hydrostatic equilibrium, the fluid is placed in a box and allowed to relax. In order to properly settle into the gravity wells created by the SPH fluid, the particles are allowed to move around and settle into an equilibrium position. In order to avoid unphysical motions, such as a smaller particle flying away or an unphysical back reaction, leading to oscillations, the particle velocities are damped such that they move, but no more than a few SPH smoothing lengths. This relaxation also allows the particles to expand or contract, by recalculating the smoothing lengths for each particle. This continues until the fluid reaches hydrostatic equilibrium. Figure 3.1 shows the particles positions in the x-y plane before and after a relaxation period of 20 $t_{\mathrm{dyn}} = \sqrt{\frac{R_\odot^3}{GM_\odot}}$ or about 10 hours. The particles on the left hand side are initially spaced in a non regular grid, and as they are allowed to relax, redistribute themselves to have no preferred axis. For clarity, Figure 3.1 only shows every 10th particle of approximately 350000.

When the stars are initially modelled in SPH, they have a very sharp radial profile in ρ, and a completely flat profile in h. As the star relaxes, the h profile adjusts to keep the number of neighbours approximately constant and ρ profile spreads out in the surface region as the particles settle into equilibrium. The deviation is very small, and has little influence over the simulation. The initial and relaxed profiles are show in figure 3.2.

In order to set up a binary star, this relaxation must be done twice, separately for each star. Close binaries experience a large tidal field, whose strength drops off at $1/r^3$, and so very close binaries will be considerably distorted with

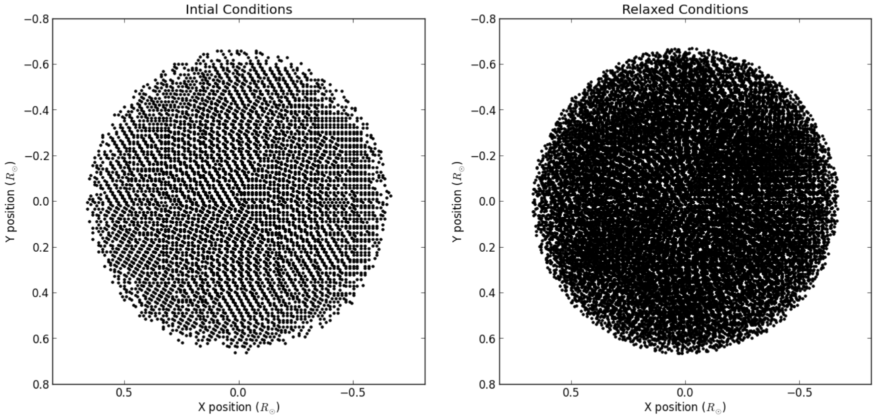

Figure 3.1: A 0.7 $M_\odot$ star before (left) and after (right) the relaxation process. The unrelaxed star has particles arranged in domains which all have a preferred axis and is unphysical when compared to a real star. The relaxed star is much more amorphous, and is a much better analogue to a real star.

large tidal bulges. In order to account for this distortion, the stars must be relaxed in their respective tidal fields. The stars are again placed in an empty box, this time at the intended orbital separation from one another. They're released, allowed to distort and then their centres of mass are shifted back to their original positions. This repeats until the new hydrostatic equilibrium is reached, but since binary stars are inherently rotating systems, it is required that the effects of the Coriolis and centrifugal forces are taken in to account, and they are part of the force balance with the tidal force, self gravity and fluid pressure. Once the stars are relaxed, the true work in evolving the equations of SPH can begin, and they are integrated forward in time, using one of the Runge-Kutta (see Ziegel et al. (1987)) schemes. Ideally, an integration scheme would be time symmetric such that the same equations can be used in reverse to integrate the backwards in time. Integration schemes with this property have the approximately the same error *per step* as non-symmetric integrators

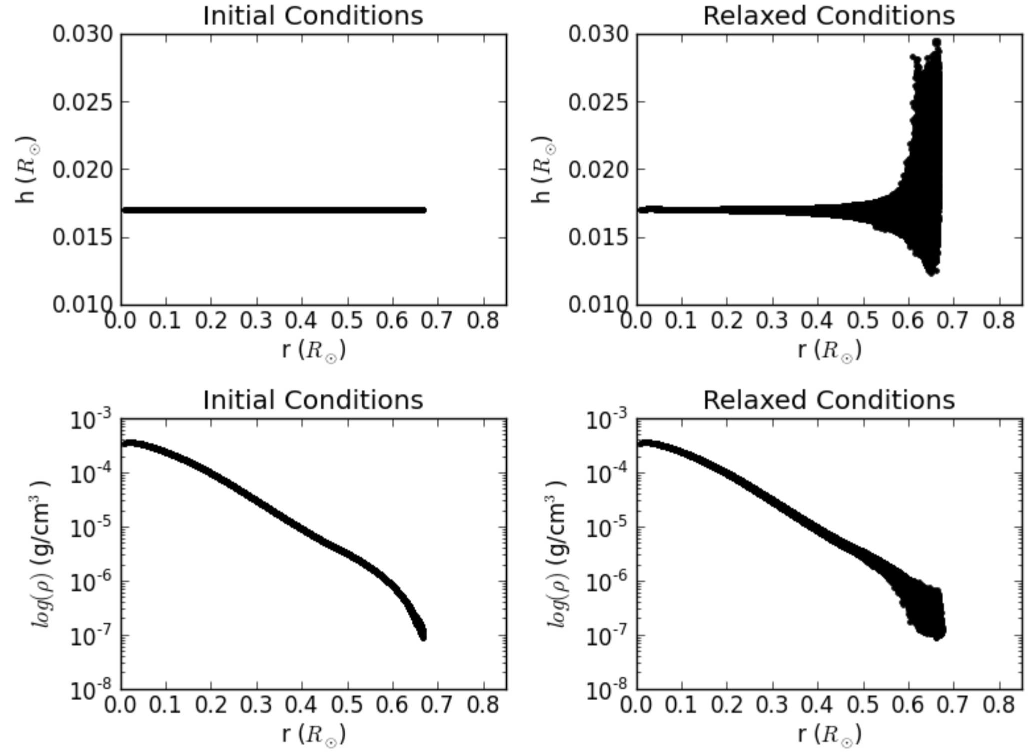

Figure 3.2: Smoothing length h and density ρ profiles of a 0.7 $M_\odot$ star before an after the relaxation process. Relaxation has a relatively unimportant role in the interior of the star, but the surface layers are much more dramatically effected. The smoothing lengths of the exterior particles must readjust in order to maintain a relatively constant neighbour number as all the particles settle into the gravitation well of the star. In log space, the density is also smeared out near the surface, but in real space this effect is not important, as these density variations are very small.

of the same order, but a smaller average error as errors tend to cancel out instead of adding. For our SPH evolution we use the code described in Lajoie & Sills (2010) which derives from the work of Bate (1995) which uses a second order Runge-Kutta scheme to integrate the equations of motion.

When the simulation evolution is complete it is time to create synthetic images, there are a number of preprocessing steps which must be completed. The bulk of the work of this thesis was designing this preprocessing workflow in order to allow for an automated calculation of synthetic photometry from a series of SPH outputs. The automation is important and helpful, as some of the preprocessing steps are reasonably time consuming.

`radmc3d` is a code which uses a grid, be it Cartesian, spherical or cylindrical, and so the first preprocessing step in to convert the SPH dumps to a grid format. In order to do this conversion, we take advantage of the visualization and processing tool, SPLASH (Price, 2013). SPLASH has access to all the variables from the SPH simulations, namely internal energy u, density ρ and smoothing length h. To convert a SPH simulation to a grid format, SPLASH sets down a box and discretizes it into $I \times J \times K$ cells, where I, J and K are the number of cells in each the x, y and z directions, respectively. Knowing the smoothing lengths, and assigning a smoothing kernel such as one of the Schoenberg B-splines, we have full knowledge of the density field at any point, based on the non-zero contributions from all the particles within 2 smoothing lengths, for the Schoenberg M4 kernel or 3 for the M6 kernel. SPLASH averages the contributions within each cell and returned a discrete grid of density and internal energy.

The accuracy of the gridding process depends strongly on the accuracy of the kernel. A higher-order kernel better approximates a Gaussian and so the particles are more heavily-weighted centrally, and while the higher-order Schoenberg B-splines extend further, their contributions are not as important. An example of this is shown in Figures 3.3 and 3.4. Here the gridded density estimate from the M4 kernel in red, shown in Figure 3.3 diverges dramatically from the SPH density profile, shown in black, whereas the higher resolution M6 kernel again in red in Figure 3.4 overlays its SPH counterpart perfectly. These plots are in code units, where the code units for density, pressure and internal energy are $\frac{M_\odot}{R_\odot^3}$,$\frac{GM_\odot^2}{R_\odot^4}$ and $\frac{GM_\odot}{R_\odot}$ respectively, where $G = 6.67384 \times 10^{-11} m^3; kg^{-1}; s^{-2}$ is Newton's Gravitational Constant, $\mathrm{R}_\odot = 695,500 km$ is the solar radius and $\mathrm{M}_\odot = 1.989 \times 10^{30} kg$ is the mass of the sun.

The internal energy is used to calculate the temperature via the equipartition theorem

$$U = \frac{3}{2} N k_b T \tag{3.1}$$

where U is the internal energy of a system of N particles with temperature T and $k_B = 1.3806488 \times 10^{-23}\ m^2\ kg\ s^{-2}\ K^{-1}$ is Boltzmann's constant. If the N particles have a mass m, N can be expressed as $m/\mu m_H$, where μ is the mean molecular weight of the fluid and $m_H = 1.67372 \times 10^{-27} kg$ is the mass of a hydrogen atom. So the temperature is

$$T = \frac{2}{3} \frac{u m_h \mu}{k_B} \tag{3.2}$$

where u is U/m, the specific internal energy. At this point we have a sphere with a density profile which agrees very well with the density profile of the star, and a temperature profile which, as shown in Figure 3.5 well models the

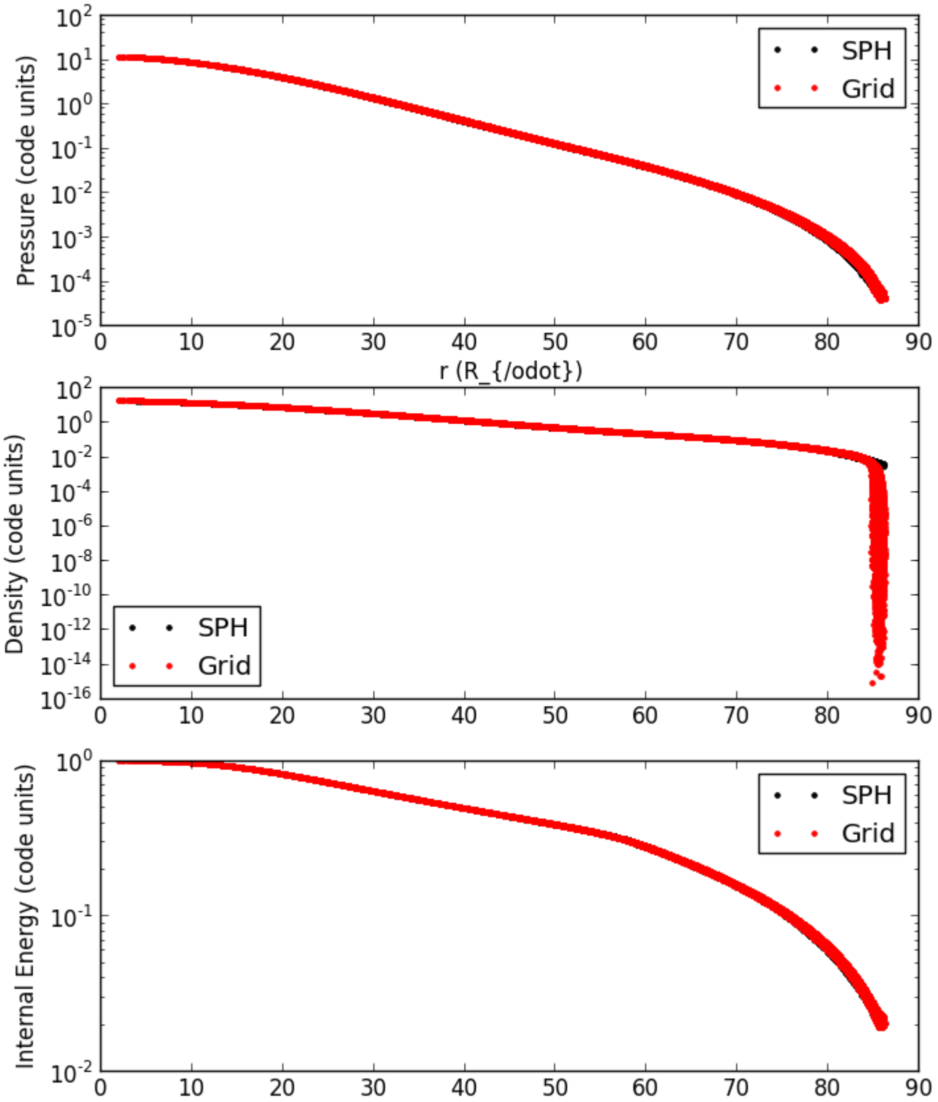

Figure 3.3: Radial pressure (top), density (middle), and internal energy (bottom) profiles as interpolated by the M4 kernel to a thee dimensional Cartesian grid with cells of side length 0.008 $R_{\odot}$. The density grid diverges wildly from the SPH model as it approaches the surface. Pressure and internal energy do not suffer from this divergence.

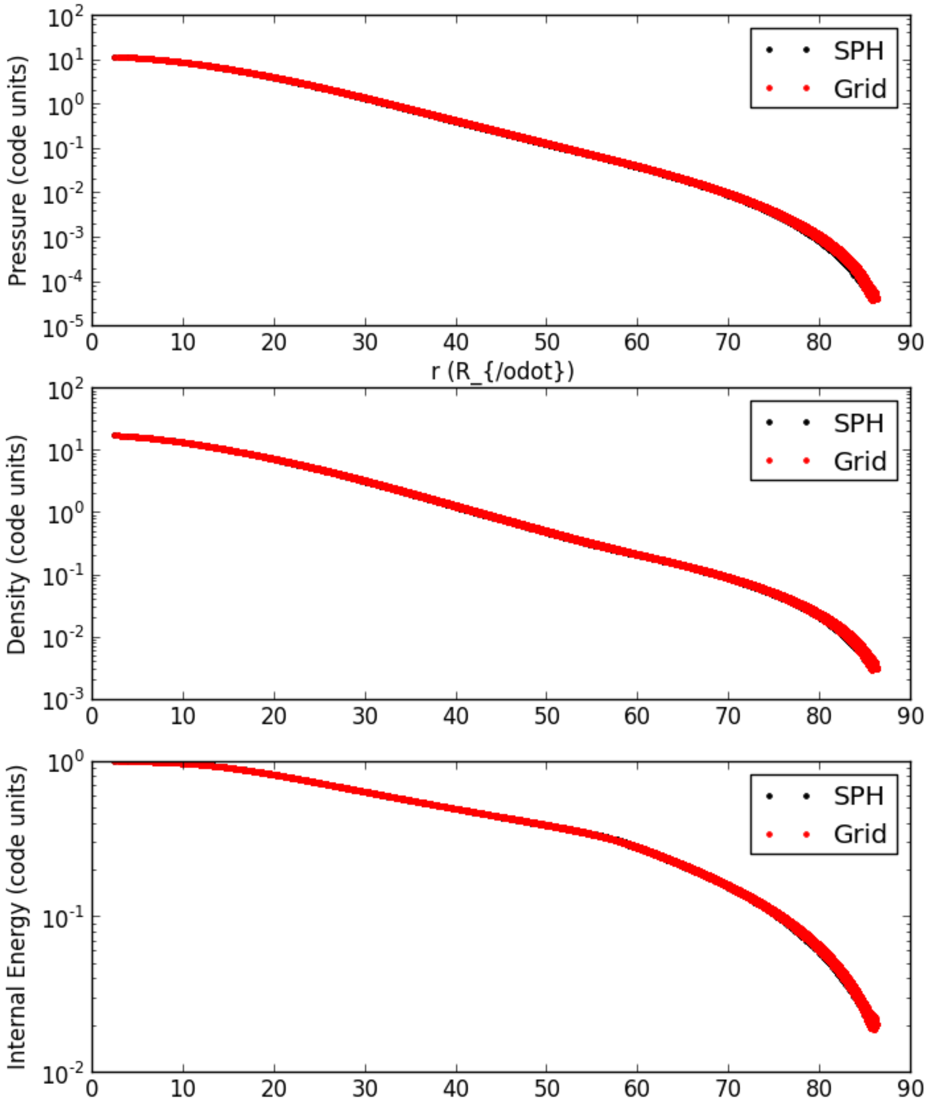

Figure 3.4: Radial pressure (top), density (middle), and internal energy (bottom) profiles as interpolated by the M6 kernel to the same grid as Figure 3.3. The higher-order kernel removes the edge divergence present in the lower order interpolation.

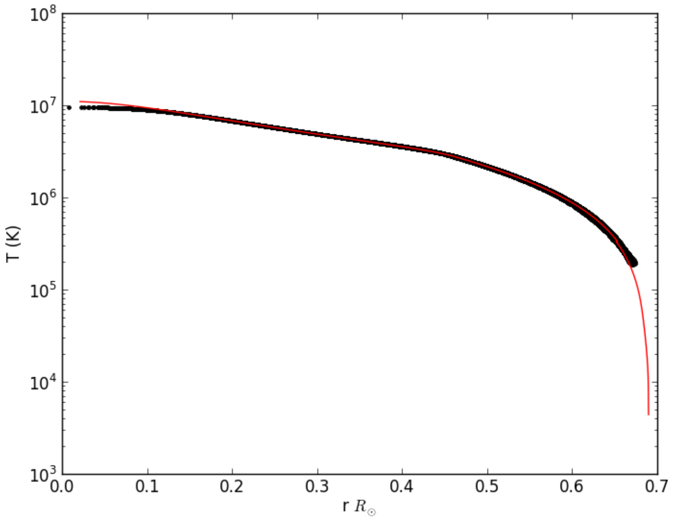

Figure 3.5: The radial temperature profile of a 0.7 solar mass SPH star shown in black with its YREC generating conditions overlaid in red. The SPH star successfully models the temperature profile from the center to very nearly the surface, but cannot resolve the outer region where the temperature drops from a few times 10^5 degrees Kelvin to the surface temperature, 4407 Kelvin in this case.

interior of the star, but cannot begin to resolve the outer layer of the star where the temperature drops by two orders of magnitude over (at most) a few percent of the total stellar radius. As a consequence, the SPH star is smaller than the YREC star by approximately the smoothing length and the "surface" temperature is far, far too high, by approximately two orders of magnitude. Interpolating the simulation to grid has no effect on this temperature profile. Unfortunately, the grid cells for any workable resolution are four to five orders of magnitude larger than the atmosphere region, which has a thickness of a few tens of kilometres, so a compromise must be made, which will be discussed in upcoming sections.

3.1 Uniform Sphere Test

At this point, some basic functionality of the method must be verified. Does the radiative transfer work as intended? Do we reproduce relatively spherical objects when we interpolate to a Cartesian grid? In order to verify both of these, a uniform sphere with a constant density of $10^{-9} g/cm^3$ and a radius of 0.2 solar radii is placed in a cubic box of side length 0.6 solar radii. A sphere of uniform brightness should emit a flux $F_\nu = \pi B_\nu(T)$ (Rybicki & Lightman, 1986) where $B_\nu(T)$ is Planck's radiation function for a blackbody in terms of frequency ν, given by

$$B_\nu(T) = \frac{2h\nu^3}{c^2} \frac{1}{e^{\frac{h\nu}{k_B T}} - 1}. \tag{3.3}$$

where $h = 6.626 \times 10^{-34}\ m^2\ kg\ s^{-1}$ is Planck's constant, $c = 2.99 \times 10^8\ m/s$ is the speed of light and k_B is again Boltzmann's constant. In order for a sphere of uniform density to be uniformly bright, it must be optically-thick. As the sphere becomes less and less optically-thick, it is no longer uniformly bright, as the edge will become more transparent, since the line of sight through the edge of a sphere is much smaller than through the centre. In order to test this, I applied a single opacity globally, ray traced an image, and then increased the opacity. The sphere starts out entirely optically-thin, and as the opacity increases, it eventually becomes optically-thick and so is expected to become uniformly bright.

The intensity emergent from a surface at a fixed temperature T is (Rybicki & Lightman, 1986)

$$I_\nu = \int_0^{\tau_\nu} e^{-(\tau_\nu - \tau'_\nu)} B_\nu(T) d\tau'_\nu \tag{3.4}$$

$$= (1 - e^{-\tau_\nu}) B_\nu(T) \tag{3.5}$$

If that surface is a sphere, we know that from equation 2.2,

$$F_\nu = \int_0^\pi \int_{-1}^1 (1 - e^{-\tau_\nu}) B_\nu(T) cos\theta d\theta d\phi \tag{3.6}$$

where θ is the polar angle and ϕ is the azimuthal angle. To simplify further analysis, we can set $\mu = cos\theta$, and $d\mu = sin\theta d\theta$.

For a perfect sphere of diameter D with a uniform density ρ, we expect the optical depth τ to be a function of μ only. The symmetry of the sphere removes any dependence on azimuthal angle, and if we consider the geometry of the problem shown in Figure 3.6 we can see that for any line of sight from the surface at point P has an optical depth of $\tau(\mu) = \tau_0 \mu$. Recall that optical depth $\tau = \int \kappa \rho dz$, and so τ_0, the optical depth along a diameter D, is simply $\tau_0 = \kappa \rho D$.

Keeping in mind the symmetry of the problem, and equation 3.6 can be simplified to

$$F_\nu = 2\pi B_\nu(T) \int_0^1 (1 - e^{-\kappa \rho D \mu}) \mu d\mu. \tag{3.7}$$

This equation can be integrated numerically, and yields a theoretical prediction for the flux emergent from the surface of a uniform density sphere with a given global opacity.

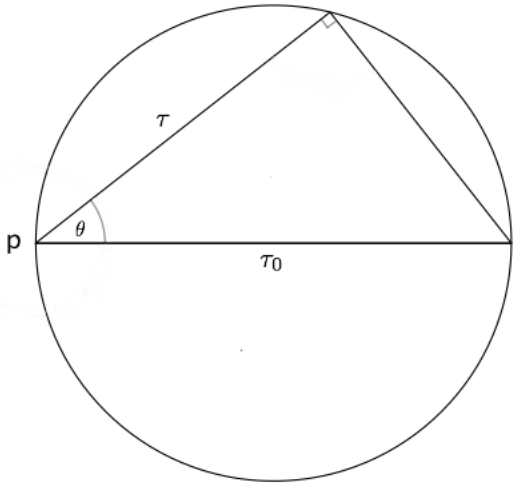

Figure 3.6: Geometry of the uniformly bright sphere when calculating brightness at point P.

Recall that this scenario was devised to test two phenomena. Primarily, we have to ensure that the radiative transfer calculations produce the expected results. But secondly, there is an additional resolution issue with the conversion from SPH to grid. It is important to know at what grid size does the radius of the gridded density field best match the initial radius from the YREC stellar model.

Results of the first part of this test are shown in Figure 3.8. In this figure the curve is normalized by the its true surface area, to compare with 3.7, so the flux plotted is

$$F_\nu = \pi B_\nu \left(\frac{A}{4\pi R^2} \right) \tag{3.8}$$

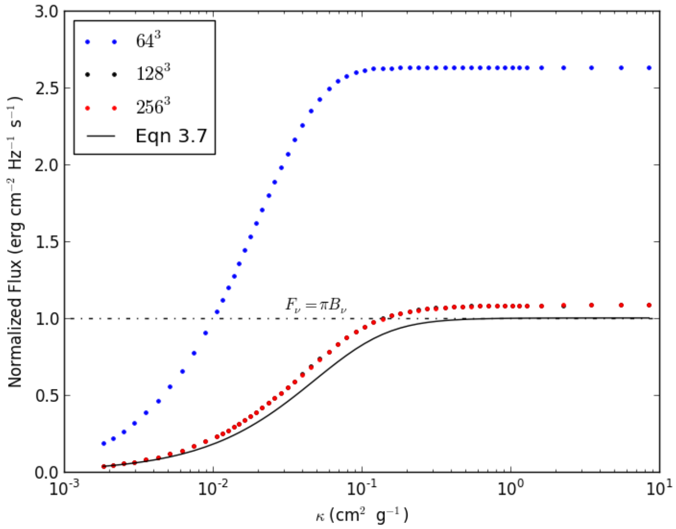

Figure 3.7: Results of uniform sphere simulations, showing convergence to the analytic prediction. The red and black points lie directly on top of one another, showing the convergence of the SPLASH interpolation to a grid with increasing resolution.

where A is the surface area of the sphere and R is its distance from the image plane.

In Figure 3.7, however, the intensities are all normalized by the actual surface area of the SPH sphere which was used to create them. Here we can see the dependence of grid resolution on flux output from the star. When interpolated to grid at low resolution, the flux output can be nearly a factor of 3 larger than what is expected, whereas higher resolutions approximate the sphere much more accurately, to within 10% or so. Figure 3.7 shows three resolutions, with 64^3, 128^3 and 256^3 cells giving cubic cells with side lengths 0.00937 $R_\odot$, 0.00469 $R_\odot$ and 0.00234 $R_\odot$ respectively. The 128^3 and 256^3 cell cases reproduce the sphere to better than 1% in area.

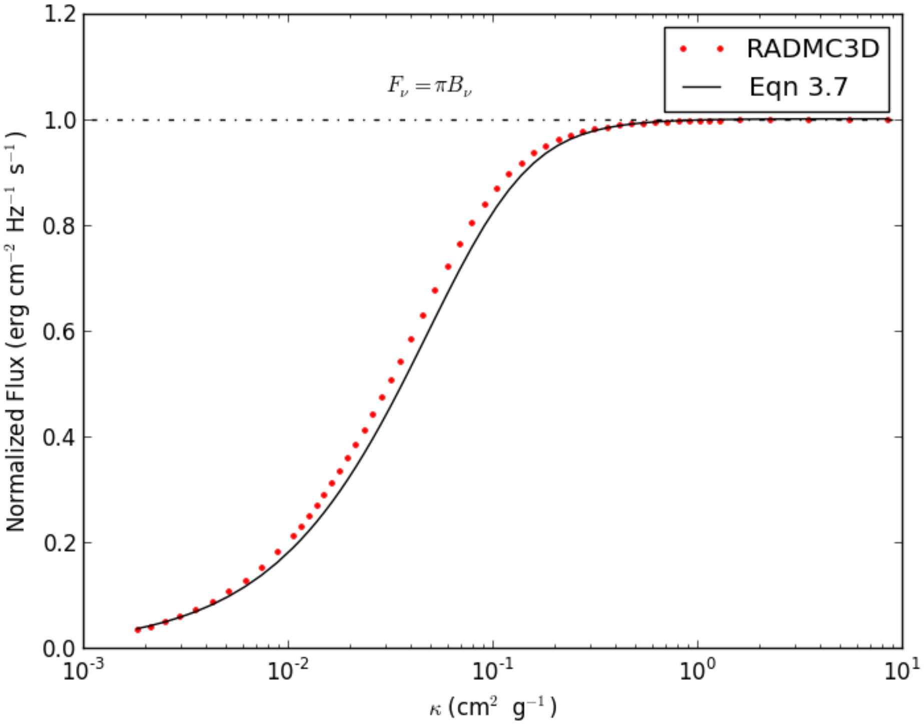

Figure 3.8: When normalized to unity, the calculated intensity curve, shown in red, very closely matches the theoretical curve, shown in black. The most important behaviour occurs as towards large κ, as the sphere becomes optically-thick.

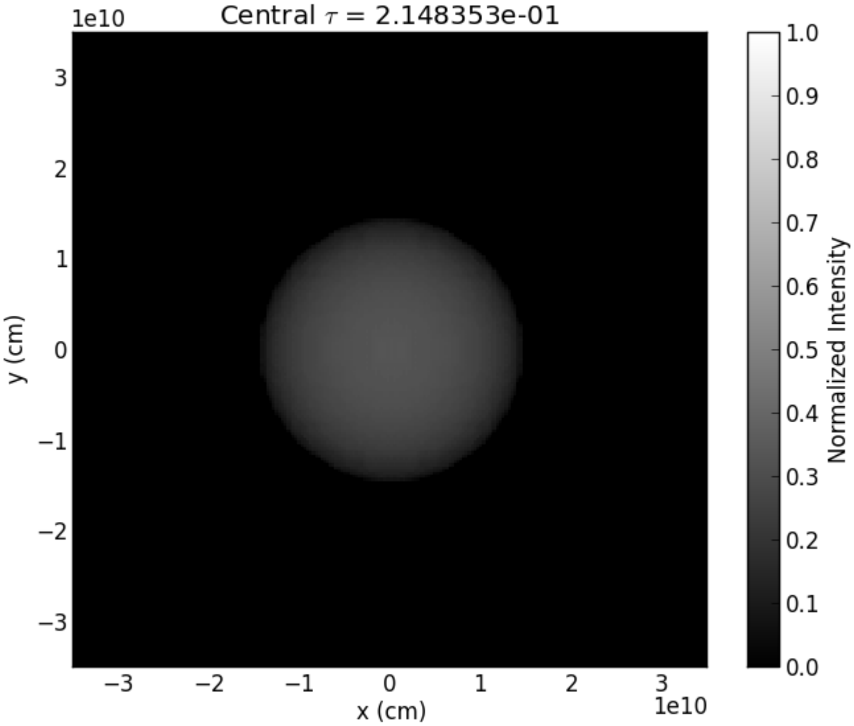

Figure 3.9: Shown here is the uniform-density sphere, imaged with a globally-applied opacity such that the central optical depth $\tau_0 \sim 0.2$ and the entire sphere is optically-thin. Limb-darkening effects can be seen along the edge, with the sphere brightening toward the centre as expected.

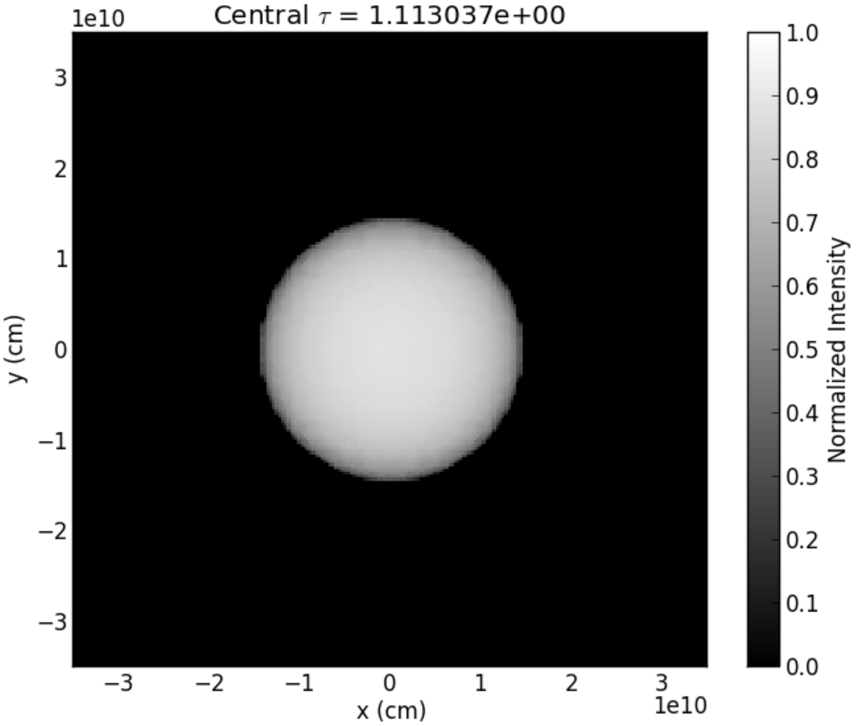

Figure 3.10: The uniform sphere, now with $\tau_0 \sim 1$. The sphere is optically-thick along the diameter, but other lines of sight are still optically-thin. Due to this, we see a central region of maximal intensity, which falls off gradually along the limbs, as expected.

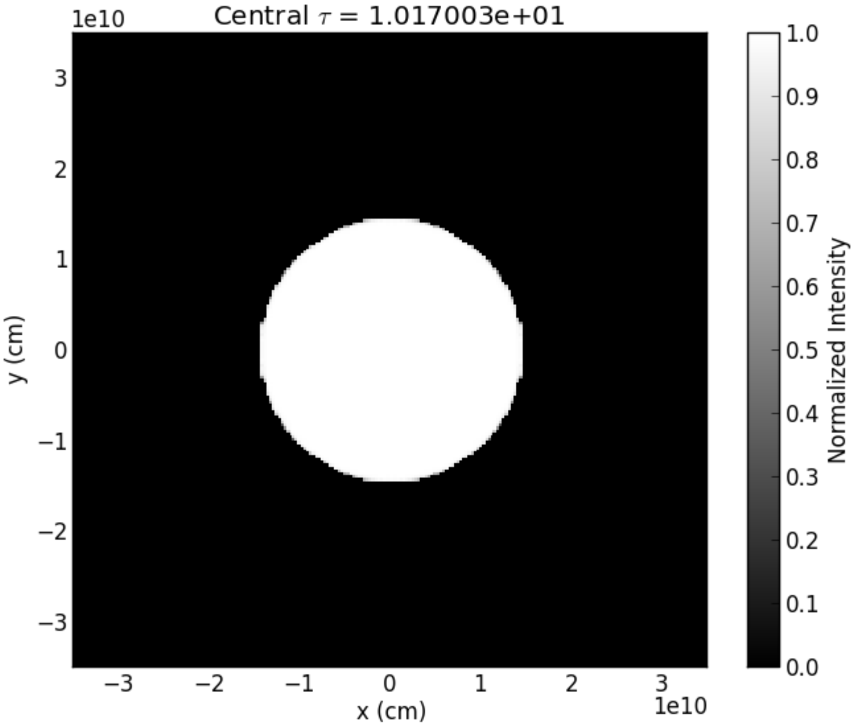

Figure 3.11: With $\tau_0 \sim 10$, the sphere is now optically-thick along all lines of sight. As expected, the brightness is uniform, with all pixels at the same intensity.

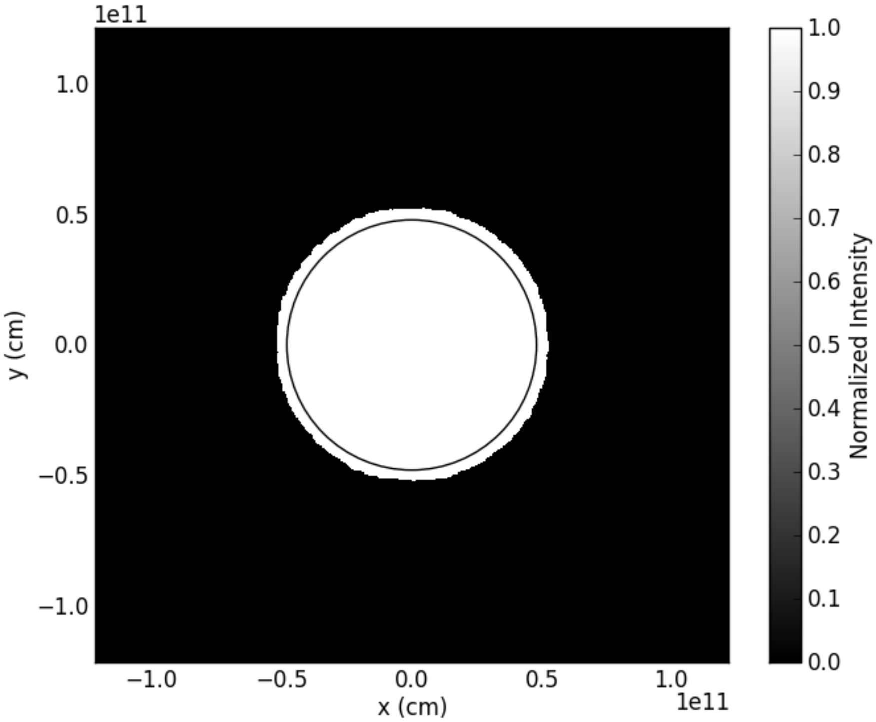

Figure 3.12: A projection of a 0.7 $M_\odot$ gridded SPH star shown in white. The star is a good approximation to a sphere, with a circular projected area. Overlaid in black in a circle of radius 0.6903 $R_\odot$, which is the true radius of the YREC stellar model which produced this star.

Snapshots of the sphere with three different opacities are shown in Figures 3.9,3.10 and 3.11. These snapshots have been chosen intentionally to show the evolution from an optically-thin sphere to one which is optically-thick and so uniformly bright. As the global opacity increases, the sphere becomes brighter along each line of sight until it reaches a maximal brightness given by its blackbody temperature of 5600 K. All cells are normalized to this brightness. This region of maximal brightness grows radially until the entire sphere is uniformly bright, as expected.

3.2 Modelling Real Stars

The previous section represents a sanity check. Without the code behaving as it should in these tests, it is impossible for any meaningful conclusions to be made. However, in addition to simply behaving as expected when compared to analytical results, we can begin to move forward. Stars are *not* uniformly dense spheres, and contact binaries have departed entirely from sphericity. Isolated stars have radial profiles of temperature which, at the centre, can reach a few 10^7 degrees K or higher, which smoothly decrease to a few 10^3 K or even a few 10^4 K in some cases. The sun, for example, has a surface temperature of approximately 5800 K, whereas the brightest star in the night sky, Sirius, is $10,000$ K (Adelman, 2004). Because the blackbody function increases monotonically with temperature, objects with higher temperatures are brighter at all wavelengths. Stars are optically-thin only for a very small percent of their radius, which sets the temperature that we see. In order to match observations any hydrodynamical stellar model must additionally be optically-thick for all rays leaving any cell which has a temperature higher than the surface temperature. Four low-mass star models, with masses ranging from 0.7 to 1.1 $M_\odot$ have been prepared to test this functionality. The models should show a blackbody spectrum with a well-defined peak, between 4000 and 6000 K, depending on their mass. Stars of this mass were chosen because they are representative of the general mass range into which the progenitors of the V1309 Sco merger fall, as modelling the photometry for low-mass mergers is the ultimate goal of this method.

3.2.1 How to build an SPH star

There exist many codes to integrate the equations of stellar structure from the interior to the surface. One such code is the Yale Rotating Stellar Evolution Code (YREC) (Demarque et al., 2007). YREC allows for the calculation of temperature, pressure, density and chemical abundances as a function of enclosed mass by using a series of concentric shells. These stellar models can be evolved from time of the zero-age main sequence and throughout their entire lifetimes. These models return information about the structure of the star from core to atmosphere. To turn these models into fluid dynamical entities in SPH, this information must be converted to three dimensions. In order to do this, the code described in Lajoie & Sills (2010) lays down a hexagonal grid of particles, in three dimensions, with pressures and densities taken from stellar evolution runs.

When the YREC models of these stars were converted into SPH, another resolution issue became apparent. The atmosphere, the region in which the stellar temperature drops to the surface temperature, is much smaller than an individual SPH particle at any tractable resolution. Approximately 300,000 particles were used in each star and the smoothing lengths were ~ 0.02 R$_\odot$, approximately two orders of magnitude larger than the thickness of the atmosphere, which is a few hundred kilometres. The main consequence of this is that the raw "surface" temperature of these SPH stars is two to three orders of magnitude higher than expected. For scale, if the sun were to be replaced with one of these model stars, its blackbody peak would be in the X-ray portion of the spectrum.

This is a major problem for synthetic photometry, which depends very heavily on temperature, and scales as T^4. It is not simple *a priori* to determine the surface temperature of a stellar object based on a temperature from the interior. The surface temperature of a star is a complicated function of the mass and radius and composition of that star. These parameters set the mode of energy transport, be it convective or radiative, the equation of state and the opacity. These are required to solve the equations of stellar structure, through which we can determine the surface temperature. Figure 3.13 shows coverage in P-ρ space of the SPH model, the YREC model from which it is generated and the MARCS atmospheres which are appropriate. It is clear there is no simple linear regression from interior to atmosphere, and while models exist they are either not applicable in general, such as individual stellar models from YREC or a similar code, or limited in scope, such as the atmosphere models which do not have adequate coverage to bridge the gap in P-ρ space. We work in P-ρ space because the specific internal energy u is calculated from pressure, using the equation of state

$$P = (\gamma - 1)\rho u \tag{3.9}$$

where γ is the ratio of specific heats. The temperature is, in turn, calculated from u using equation 3.2. P and ρ are the important variables in the SPH simulation, and so it make senses to look at things in this space.

In this section I will present a method to determine surface temperatures and relevant opacities from a given interior model, given by a hydrodynamic code, using the equation of hydrostatic equilibrium and the MARCS model stellar atmospheres. The method is relatively simple and uses the same ideas

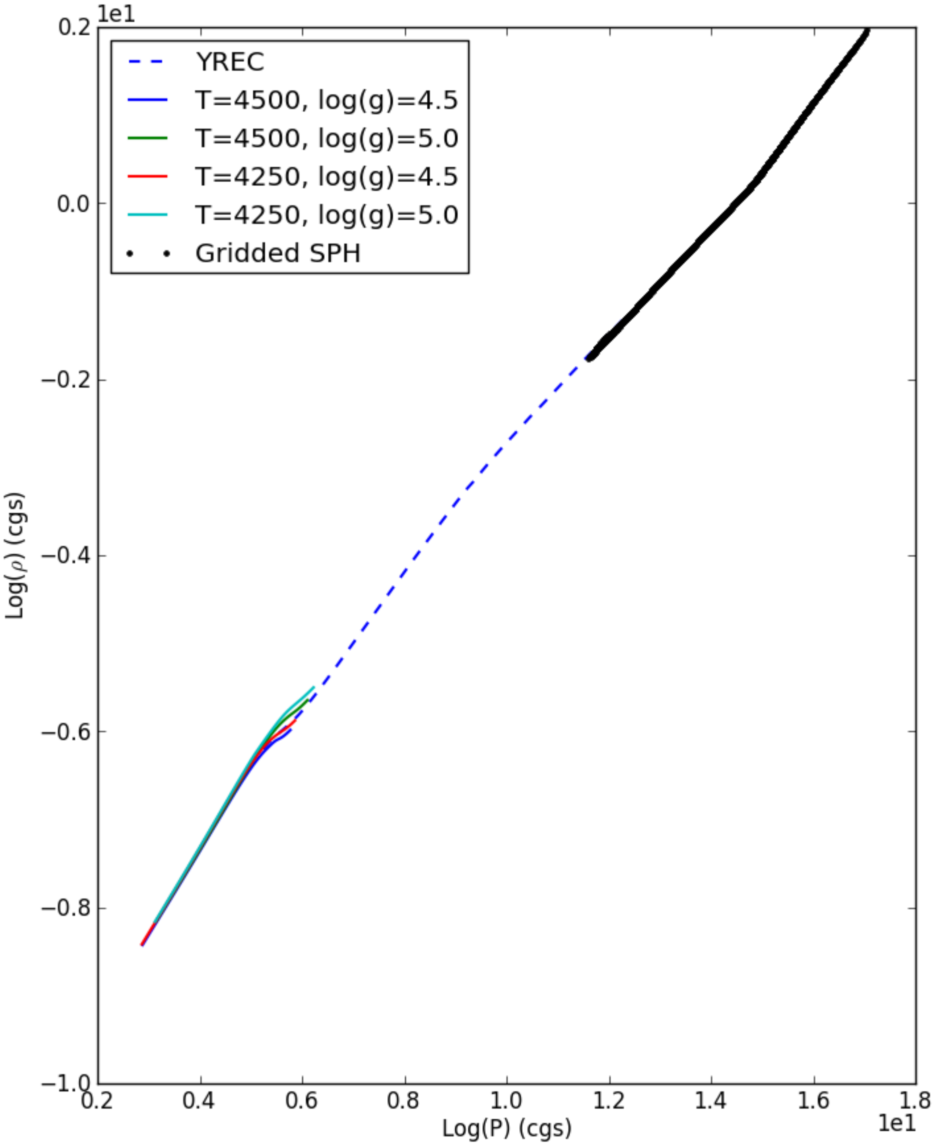

Figure 3.13: Shown in black is the gridded SPH model of a 0.7 $M_\odot$ star with T_{eff}=4407 K and log(g)=4.6. The blue dashed line shows the YREC model of the same star, and the four solid lines show the 4 most appropriate MARCS atmospheres for this stellar model, forming a regular grid around it in T-log(g) space.

used in stellar structure codes to determine the actual structure of the atmospheres. As such, it is far more generally applicable than a linear regression or a parametric fit.

3.2.2 Temperature Extrapolation

To properly determine a more appropriate surface temperature, we take advantage of the large resolution in pressure between the outermost layer of the SPH star and the $\tau = 2/3$ layer of the MARCS atmospheres. The change in mass in this region is negligible compared to the mass of the star, but the pressure changes by serveral orders of magnitude. Taking the assumption of hydrostatic equilibrium where

$$\frac{dr}{dP} = -\frac{r^2}{GM_{enc}\rho} \tag{3.10}$$

we can integrate inwards from the MARCS atmosphere models to link up with the SPH model. To get a sensible average and to account for possible outliers, we take the average pressure P_{SPH}, distance from the center of mass r_{SPH}, density ρ_{SPH} and smoothing length h, of the outermost 0.1% of particles. For systems of multiple stars, P_{SPH}, r_{SPH} and M_{enc} are calculated separately for each star. In contact systems, the particles are shared between stars, and to approximate sphericity, particles are associated with one star or the other depending on which side of the center of mass of the system they lie on. From this, effective values of P_{SPH}, r_{SPH} and M_{enc} can be calculated. The SPH stars are on average larger than their initial YREC conditions by an additive factor of about a smoothing length. All of this allows us to numerically integrate the equation of hydrostatic equilibrium

$$\int_{\mathrm{r_{SPH+h}}}^{r_{\mathrm{SPH}}} dr = \int_{P_{\mathrm{MARCS}}}^{P_{\mathrm{SPH}}} \frac{dPr_{\mathrm{SPH}}^2}{GM_{\mathrm{enc}}\rho}. \tag{3.11}$$

In order to calculate ρ, we must chose an equation of state. A convenient and, more importantly, relevant equation of state for this region of a star is

$$P = A\rho^{\gamma} \tag{3.12}$$

where A is a constant and γ is the ratio of specific heats. To use this equation of state, we calculate A using the values of P and ρ from the MARCS atmosphere models and a γ of between 1.4 and 5/3. γ varies across this range due to the ionization of hydrogen. As hydrogen becomes more and ionized in the outer layers, the equation of state of the gas changes. The MARCS atmosphere catalogue has excellent coverage in the range of low mass stars, with a $T \in [3000K, 8000K]$, spaced approximately every 250 degrees and $log(g) = (4.0, 4.5, 5.0)$. This gives approximately 60 atmosphere model covering the entire sensible range of (T,log(g)) the low mass stars we are considering in this chapter.

This integration produces a P-ρ profile which approximates well the expected profile from YREC. Shown in Figure 3.14, is the success of this model in bridging the gap in P-ρ space between the MARCS model atmospheres and the SPH model for the case of the 0.7 $\mathrm{M}_{\odot}$ model. In general, this integration must be repeated for each atmosphere. The integrated atmosphere models are then are then grouped into adjacent pairs. An adjacent pair of atmospheres differ in both surface temperature and surface gravity, but are within one step of one another. This is because in general we do *not* know the actual surface temperature and surface gravity of the star, and so we must test each pair of atmospheres find those which are most suitable.

Using the pressure and density profiles integrated inward from the proposed atmosphere to the surface of the star, how do we determine surface temperature? In order to find temperature and surface gravity, we can assume that pressure is a function of T and $log(g)$ such that

$$P = aT + b\ log(g). \tag{3.13}$$

Each atmosphere integration will produce a (P,$\mathrm{T_{eff}}$, log(g)) triplet, where P is the pressure at the depth of the outermost SPH particle. Using the triplets from adjacent pairs of atmospheres, we have can determine a and and b, which can then be used to determine T_{eff} and $log(g)$ from the pressure of the outermost SPH particle via a bilinear interpolation. In this way, we are determining the surface temperature of the star based on its interior structure in a realistic manner. The surface gravity in this interpolation is redundant, as

$$g = \frac{GM_{enc}}{r^2} \tag{3.14}$$

which is used in the integration of the equation of hydrostatic equilibrium. Nonetheless, we can use the $log(g)$ from this interpolation equation later to help quantify the error in our interpolation, and to determine which atmospheres are the most appropriate. After these integrations and interpolations have been performed for each atmosphere, we have P_{int} and ρ_{int} at the same distance from the center of mass as P_{SPH} and ρ_{SPH}, and also $log(g_{\mathrm{int}})$, which

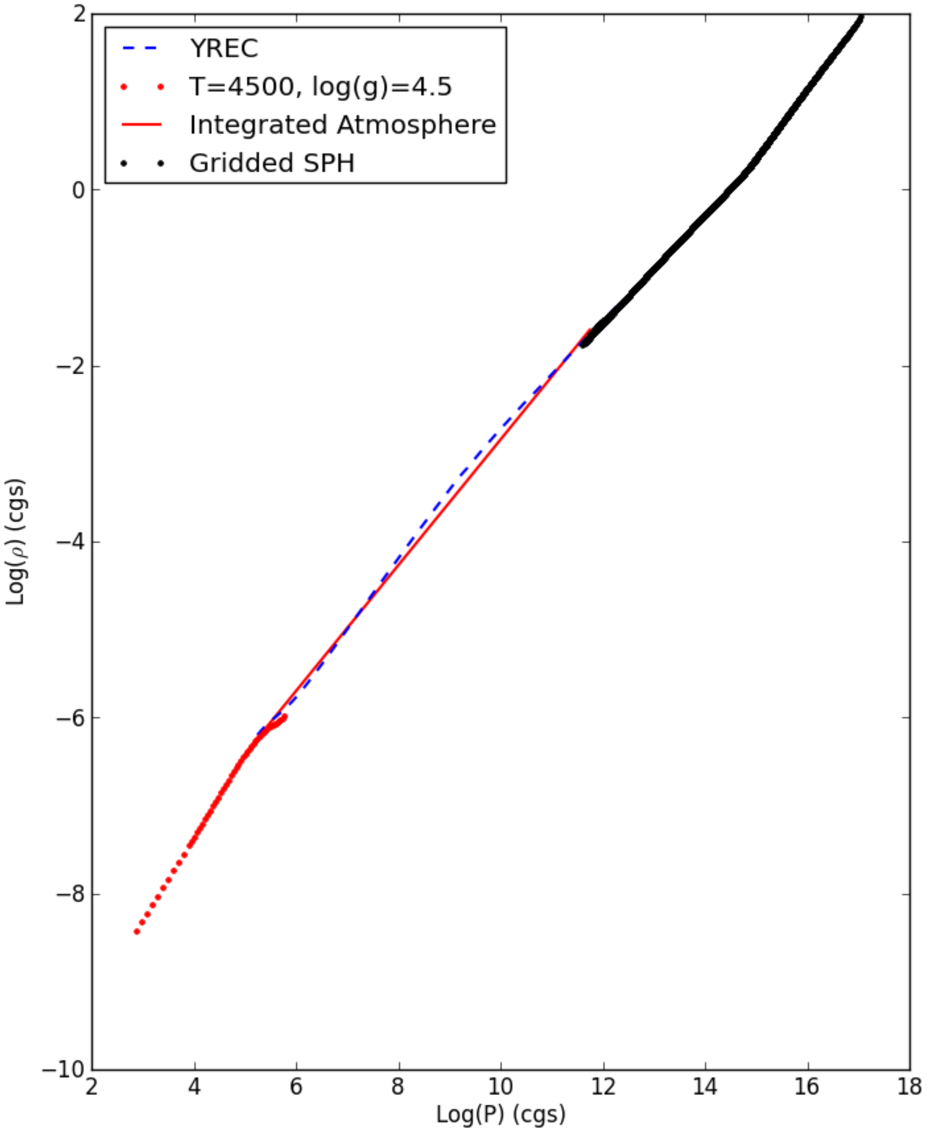

Figure 3.14: P-ρ profiles from YREC, Gridded SPH simulations, MARCS model atmospheres and the integration described in this section. The YREC model shown in the dashed blue line is that of a 0.7 $M_\odot$ star, which, when interpolated to SPH (black), does not resolve the red circles of the MARCS model. The red line is the integrated atmosphere, with initial integration points taken from the pictured MARCS atmosphere. The integration successfully links the atmosphere model and the SPH result.

should compare well to $log(g_{\rm SPH})$. To determine the most appropriate atmosphere, we minimize the relative error δ in these three quantities where

$$\delta = \frac{|P_{\rm SPH} - P_{\rm int}|}{P_{\rm SPH}} + \frac{|\rho_{\rm SPH} - \rho_{\rm int}|}{\rho_{\rm SPH}} + \frac{|log(g)_{\rm SPH} - log(g)_{\rm int}|}{log(g)_{\rm SPH}}. \tag{3.15}$$

Shown in Figure 3.15 is δ for the entire range of interpolated atmospheres of the 0.7 $M_\odot$ star. δ determines a temperature within ~10% of the actual $T_{\rm eff}$ of the star for all models. The four models tested above are all systematically hotter than expected, but further work is required to determine if this is a general systematic trend.

3.2.3 Opacity

The final required input to `radmc3d` is the stellar opacities. Opacities can be either grey or monochromatic, and can include the effects of scattering. The MARCS model atmosphere provide opacities, both scattering and absorption at over 1000 wavelength points in the region of the EM spectrum relevant to low mass stars, ranging from 90 to 200,048 nm. To properly determine the opacity based on the interpolated temperature, recall that a given model atmosphere depends only on temperature and surface gravity, which are two quantities we now have. The simplest bilinear interpolation in a two dimensional plane involves first interpolating in one dimension, such as T, and then interpolating again in a perpendicular direction, in this case $log(g)$. Doing this interpolation at every wavelength point for both scattering and absorption opacities gives a full, wavelength-dependent opacity function for our new interpolated atmosphere. Since, due to limits of resolution, each cell is very

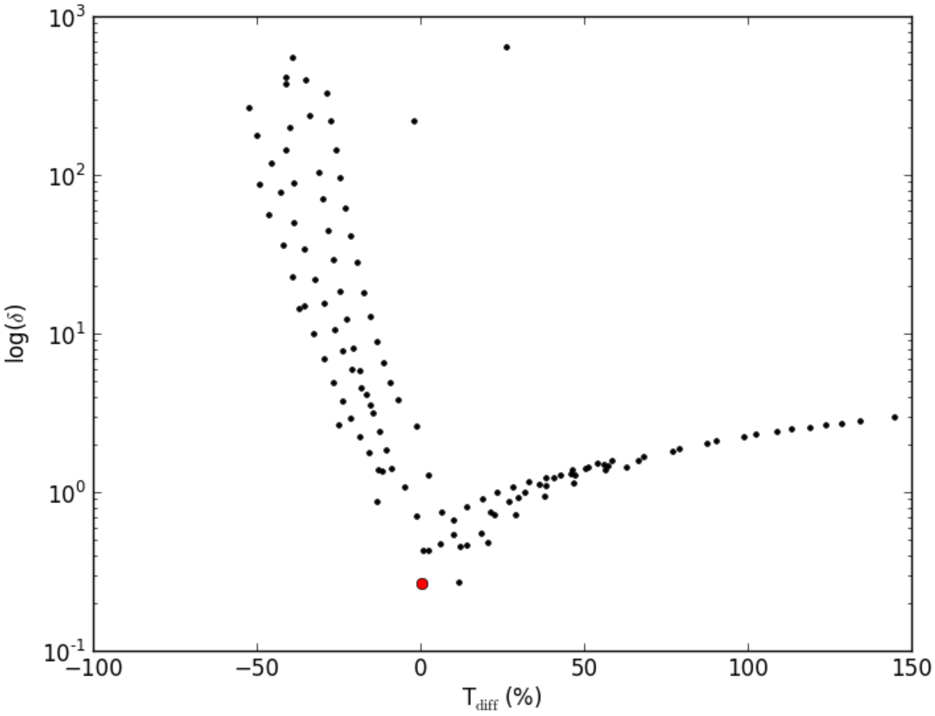

Figure 3.15: Error quantity δ plotted as a function of $\frac{T_{\mathrm{interp}}-T_{\mathrm{eff}}}{T_{\mathrm{eff}}}$ for the 0.7 $M_{\odot}$ star. The other models of stars produce similar results. δ rules out higher temperature atmospheres very effectively, but there can be some redundancy in atmospheres which have similar interpolated surface temperatures. The temperature selected by error minimization is indicated in red.

optically-thick, it is reasonable to apply this opacity to all cells, even though it is truly valid only at the surface.

This simplification is justified because in `radmc3d`, if a photon sees an optical depth along its path of greater than 10, it is considered to be trapped forever, and its propagation is no longer tracked. As shown in Figure 3.16, there are two layers in the star from which photons can escape. Obviously, from the outermost layer of cells, outside of which the density is zero, photons can stream outward in all directions. Any photons which attempt to travel into the interior of the star will be lost forever, as they will see a large optical depth. The optical depth across a single cell is typically greater than 100. Consider, however, a second layer of cells, one step in from the exterior layer. As shown in Figure 3.16, these cells can often have a diagonal line of sight through which a photon can escape unimpeded. All other photons will never escape. Therefore, we set the temperature of the two outermost cells, as shown in Figure 3.16, to be that determined by the interpolation using equation 3.15. The following section will verify the validity of this method with a series of tests on stellar models.

3.3 Stellar Temperature Tests

The temperature of a star, along with its radius, are the most important factors in setting the flux emitted from that star. The spectrum of the star is imprinted by the composition, and studying variations in this composition is the basis of spectroscopy. These variations in composition on both global and local scales will change the individual spectral fingerprint by adding or

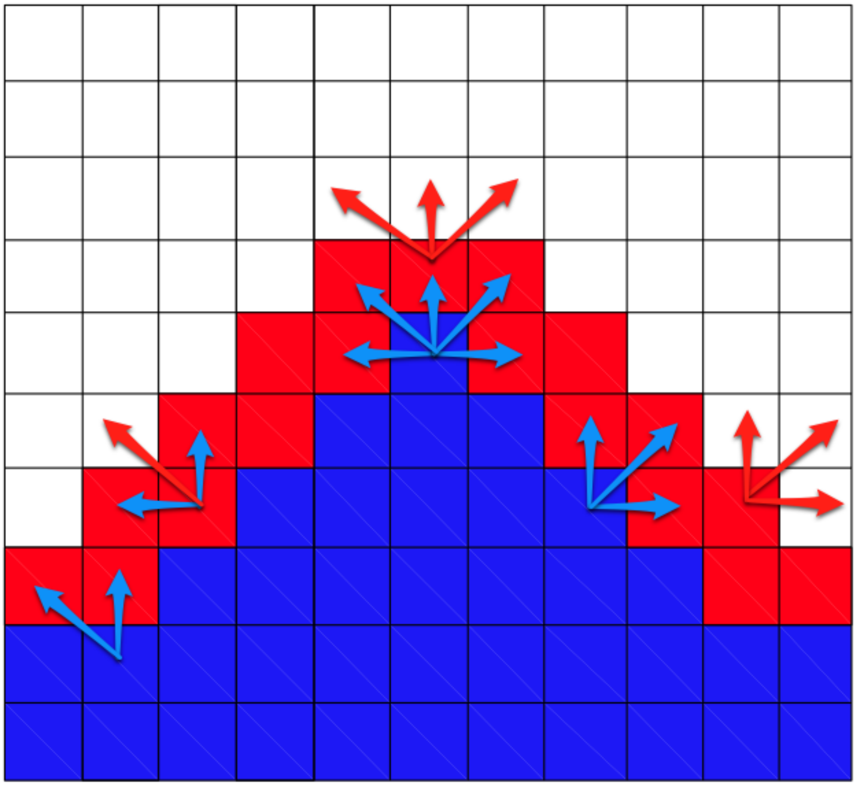

Figure 3.16: Shown in blue are cells from which photons will never escape, whereas red cells have the possibility of a photon escaping. The blue arrows are the directions in which a photon could be emitted which would never escape, whereas the red arrows are photons which can escape. Note that for the inner layer of red cells, photons can escape along the diagonal, as shown by the red diagonal arrow.

removing lines and bands. The depth and width of these lines is again strongly dependent on temperature, in addition to pressure and composition. Without accurate estimate of temperature, it is impossible to do meaningful synthetic photometry, and any attempt at synthetic spectroscopy is out of the question. Synthetic spectroscopy would be a useful tool for example in an attempt to quantify the rotational properties which would be observed after a merger, or, with the help of software beyond the scope of this work, chemical evolution in a possible excretion disk, formed post-merger which could be of interest considering the results of Nicholls et al. (2013). However, this work is limited to photometry only, with no individual spectral lines included. The following section will verify that the method outlined in the previous section is accurate for real stellar models, allowing for reliable photometric calculations.

In order to test that the corrected temperatures are within a reasonable range, such that an FGK type star does not have a predicted temperature of 100,000 degrees Kelvin, and appear as an O type star, or in the other direction, as an M type star with an effective temperature of 2500 degrees Kelvin, we have a series of 4 stellar models, ranging in mass from 0.7 solar masses, to 1.1 solar masses. The stellar models were evolved in YREC for 10 Gyr. This is approximately the main sequence lifetime of the 1.0 and 1.1 solar mass models, and so these stars have just begun to turn off the main sequence. Ideally the method should not be sensitive to evolutionary state.

Each models was interpolated from SPH to a three-dimensional Cartesian grid with 128^3 pixels in square boxes of side length between 2.0 $R_\odot$ for stars with masses 0.7 $M_\odot$ and 0.8 $M_\odot$, and 4.0 $R_\odot$ for the higher-mass stars with

M= 1.0 $M_\odot$ and 1.1 $M_\odot$. This difference is to account for expansion as the higher-mass stars have begun to swell onto the giant branch. This gives grid cells with side length of 0.01563 and 0.03125 solar radii, respectively.

Figure 3.17 shows the agreement between the emergent flux and a blackbody at the same temperature. Blackbody spectra were obtained for all 4 stars using both the temperatures determined from the method described in the previous section and the actual surface temperatures determined in the YREC modelling stage. Figure 3.17 shows as an example the predicted temperature spectrum of the 0.7 $M_\odot$ star. All of the spectra, both with interpolated temperatures and with real temperatures match the blackbody spectrum at that temperature to better than 0.1% . `radmc3d` beautifully images these stars as perfect black bodies at any temperature which is assigned to the surface layers.

Some other important results of this test are summarized in Table 3.3. The theoretical integrated flux of a blackbody is

$$F = \sigma T^4 \tag{3.16}$$

where $\sigma = 5.670 \times 10^8 \ W \ m^2 \ K^4$ is the Stefan-Boltzmann constant. These theoretical fluxes are all accurate to within 30%, which this is the same as saying that temperature are accurate to within 10%, as shown in Table 1. Of particular interest for the merger of V1309 Sco is the I band flux, as the OGLE microlensing project was an I band survey. I band fluxes are accurate to better than 25%. The I band fluxes are more accurate than the global fluxes because the red tail of the blackbody spectrum is not as sensitive to these temperatures. The hydrodynamic models are all larger in radius than the YREC models used to create them, but interestingly, stars with larger

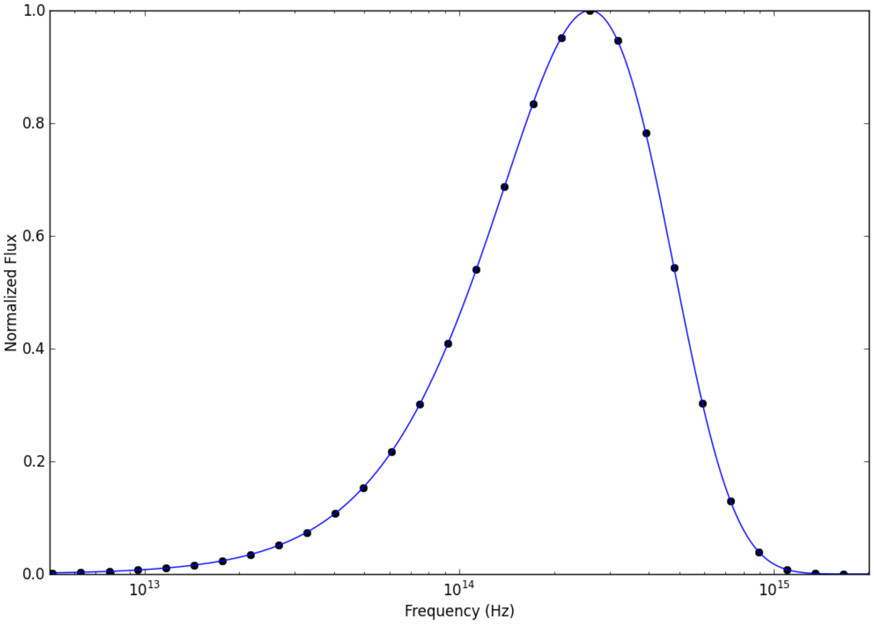

Figure 3.17: Interpolated spectrum of 0.7 $M_\odot$ star with associated blackbody spectrum at the same temperature in blue. All spectra for all stars produced equally good agreement with theory.

Mass ($M_\odot$)	T_{eff} (K)	T_{interp}(K)	Global ΔF (%)	I band ΔF (%)	ΔA
0.7	4407	4423	1.46	1.51	19.0
0.8	5023	5219	16.5	14.9	12.3
1.0	5754	5864	7.87	6.34	1.69
1.1	6025	6451	31.4	23.2	1.68

Table 3.1: Summary of results of single star surface temperature integrations

errors in temperature have a tendency to have a smaller error in projected area, causing the relative error in I band luminosity to be better than 25% in all cases.

To test for numerical convergence, the resolution was doubled from 128^3 to 256^3 grid cells. All the results shown in Table 3.3 were consistent when the resolution was doubled.

3.4 Binary Star Orbits

With the surety that the single stars reproduce their expected blackbody spectra with good accuracy, it is now time to test this method in the regime for which it was designed: binary stars. To reproduce binary star photometry correctly, each star needs to be opaque to the radiation from the other star, and the relative areas of the stars must be such that we can accurately reproduce the expected depths of transits, both as the primary passes in front of the secondary and vice versa. Consider a primary with luminosity L_1 and surface area A_1 and a secondary companion with luminosity L_2 and surface area A_2. Since flux $F = L/A$, for the majority of the orbit, the flux emitted from the system will be $F = L_1/A_1 + L_2/A_2$. When the larger primary passes in front of the secondary, we expect a flux of $F = L_1/A_1$. Finally, when the secondary passes in front of the primary, we expect a flux of $F = L_1/(A_1 - A_2) + L_2/A_2$. These dips in flux are characteristic of a detached binary system. A contact system will have similar extrema, but with broader rises to maxima and slower decreases to minima.

To test the method in this regime, we've devised three test cases. First we consider an equal-mass, detached binary. Both stars in this system have a mass of 0.7 $M_\odot$ and a separation 4.0 $R_\odot$ and 512 grid cells in each direction in a 6.0 $R_\odot$ box, yielding side lengths of 0.0117 $R_\odot$. Second, we model an unequal mass system, comprised of a primary with a mass of 1.1 solar masses and a secondary of 0.7 solar masses, with the same separation and resolution. And finally, we looked at a contact binary, with components of mass 1.1 and 0.7 solar masses at the same resolution again. Contact binaries have a very distinct light curve, and reproducing such a light curve is crucial for any future efforts to model contact binary evolution. To compare with these results, theoretical light curves were produced using the `shellspec` code, outlined in Budaj & Richards (2004). `shellspec` uses a grid to calculate light curves, spectra and images of stars with jets, disks and companions immersed in an optically-thin interstellar medium. `shellspec` light curves are produced using the same parameters for temperature and radius that are present in the fully processed, gridded SPH results which are fed into `radmc3d`, including the inflated radii and the interpolated surface temperatures.

Shown in Figure 3.18 is the light curve from the equal-mass binary. As expected, the minima due to the eclipses are equal in depth, as the two stars present the same projected area to the observer and completely occult one another as well as emitting identical fluxes. An artifact of the gridding process is evident at each quarter phase in both `radmc3d` and `shellspec` results. These light curves are produced by rotating a static binary system through 360 degrees, and therefore it is expected that certain grid artifacts, particularly when looking down an axis of the grid, will be present. The grid cells are all cubic in shape, and as a cube rotates, its projected area onto a plane perpendicular to the line of sight is smallest when looking directly at a face. Figure 3.19 shows an image of a single eclipse, where one star has completely blocked out the light from another identical star.

The unequal-mass binary shows a similar, though distinct light curve in Figure 3.20, where the two eclipses are of different depths. This system has the same orbital separation as the equal mass system, but has a primary with a mass of 1.1 $M_\odot$ and a secondary with a mass of 0.7 $M_\odot$. When the lower surface brightness secondary passes in front of the primary, as shown in Figure 3.21, less light is observed than would be emitted from a the primary star alone. When the secondary passes behind the primary, it is completely occulted and so the flux incident on an observer is simply the flux emitted from the primary. This explains the unequal depth of these eclipses.

The final test of this method is in the non-spherical regime of a contact binary. Can we accurately predict a temperature for a contact binary, and will it produce the kind of light curve that we expect? Predicting the real temperature is difficult, as there is some mechanism of heat transfer occurring in the system that is poorly understood (see Webbink (2003) and references therein) and not included either in SPH or in radiative transfer modelling.

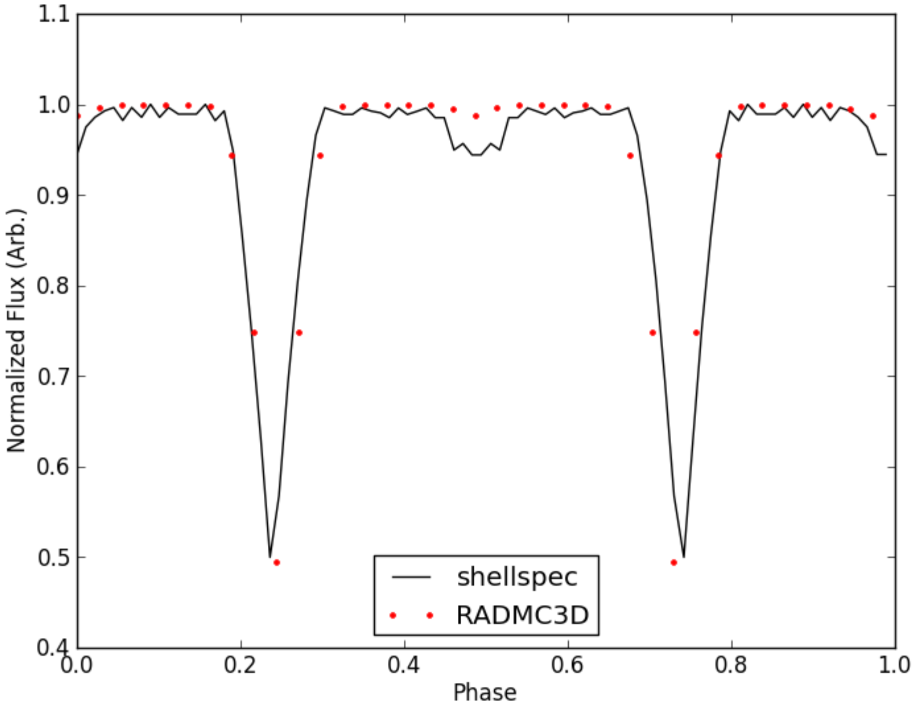

Figure 3.18: The normalized light curve from the equal-mass binary calculated using `radmc3d` shown in red. Two 0.7 $M_\odot$ stars orbit one another with an orbital separation of 4.0 $R_\odot$ and complete one orbital period, showing two eclipses of equal depth. The black line is the `shellspec` light curve.

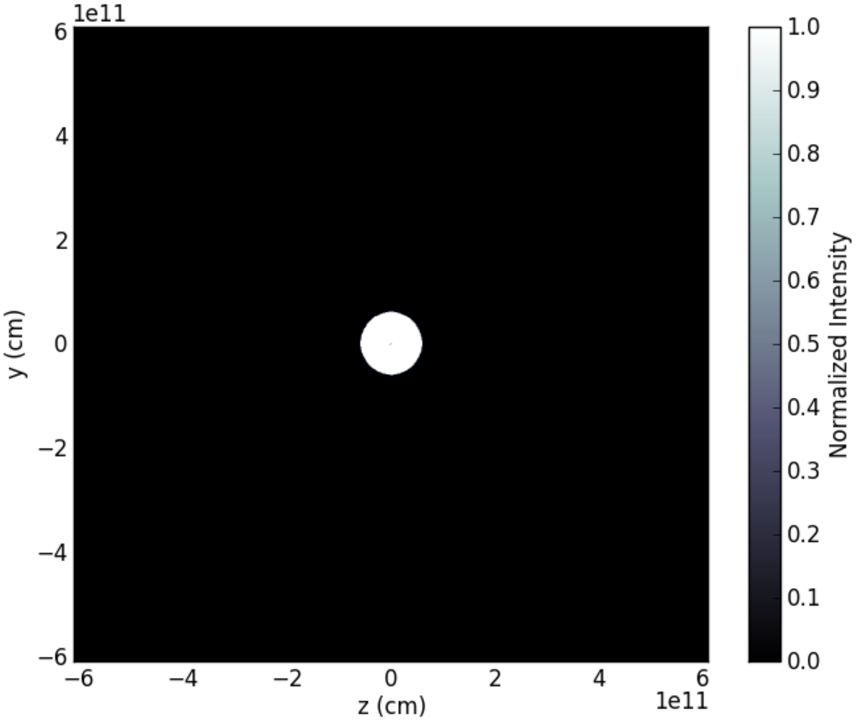

Figure 3.19: An image of an eclipse of the equal-mass binary system. A single object is visible, as both stars project the same area onto the sky.

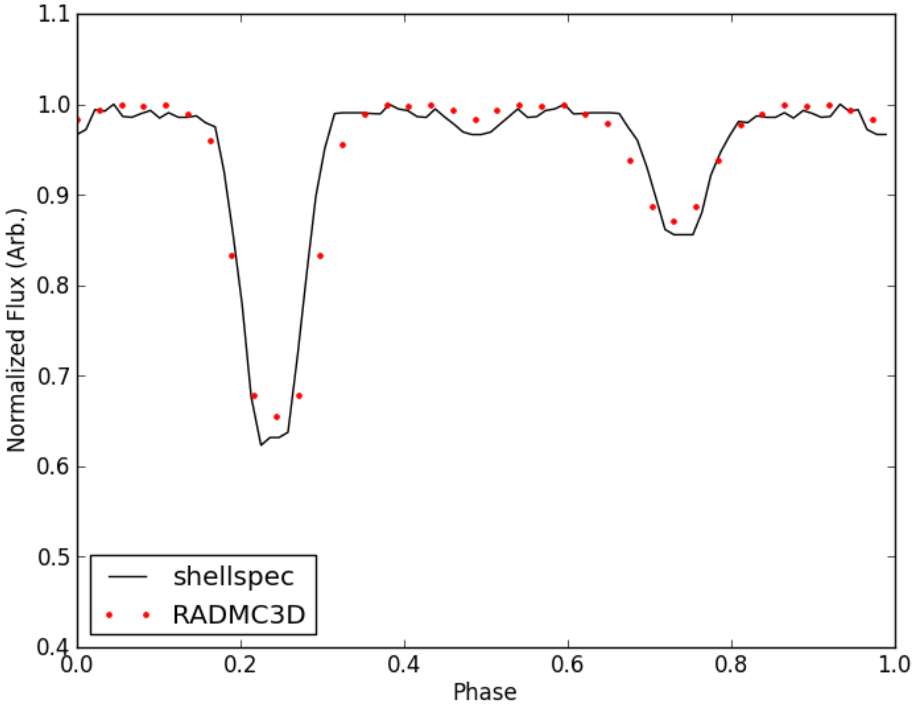

Figure 3.20: The normalized light curve of the unequal-mass binary calculated using `radmc3d` shown in red, consisting of a 1.1 $M_\odot$ primary and a 0.7 $M_\odot$ secondary at the same orbital separation of 4 $R_\odot$. The unequal eclipse depths are clearly shown, due to the difference in area and brightness of the two stars. The black line is the `shellspec` light curve.

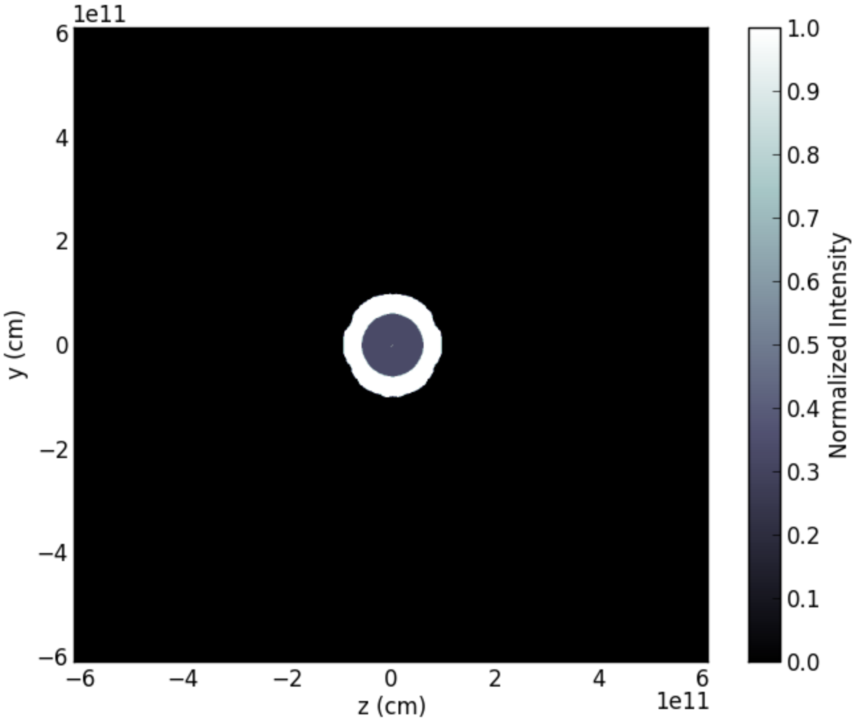

Figure 3.21: An eclipse of the unequal-mass binary. Clearly shown is the dimmer secondary star passing in front of the primary star, leading to the deeper minimum in the light curve. This is due to differing surface brightness of the two stars.

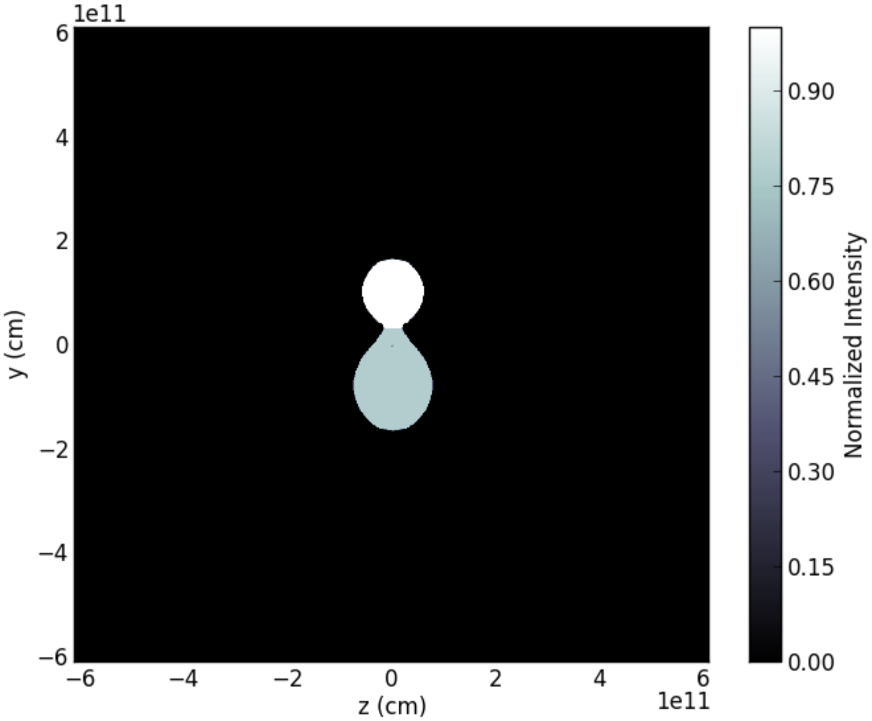

Figure 3.22: A side-view of the 0.7 and 1.1 $M_\odot$ contact binary. The system presents the expected "peanut shape" defined by the Roche potential.

Our hydrodynamic models assume that each star is separately in hydrostatic equilibrium, and there is no mechanism for the kind of heat transfer thought to equilibrate the surface temperatures of these stars.

The interpolated surface temperatures for the 1.1 $M_\odot$ and 0.8 $M_\odot$ components of the contact binary shown in Figures 3.22 and 3.23 are T_1=3361 K and T_2=3564 K respectively. Figures 3.22 and 3.23 show the side and eclipsing views of the binary orbit, respectively. These are phenomenologically consistent with the understanding of contact binary stars, where the physically smaller and less massive star tends to be hotter, and joined to the other star in a peanut shape by the Roche potential. The sharp gradient between one star and the other is due to the temperature calculation, and is approximately at the center of mass.

The photometric light curve, shown in 3.24 is in excellent agreement with expected theory. All three light curves are accurate to within the scatter of the `shellspec` curves, and the contact binary is accurate to better than 5%. The large scatter in the `shellspec` curves is due to an inherently lower resolution. The method reported here allows for high (512^3 pixels is easily doable) resolutions, whereas `shellspec` has trouble with 90 pixels in a given direction. The source of this resolution issue is unclear, but it shows the robustness of directly imaging hydrodynamic simulations via a code such as `radmc3d`.

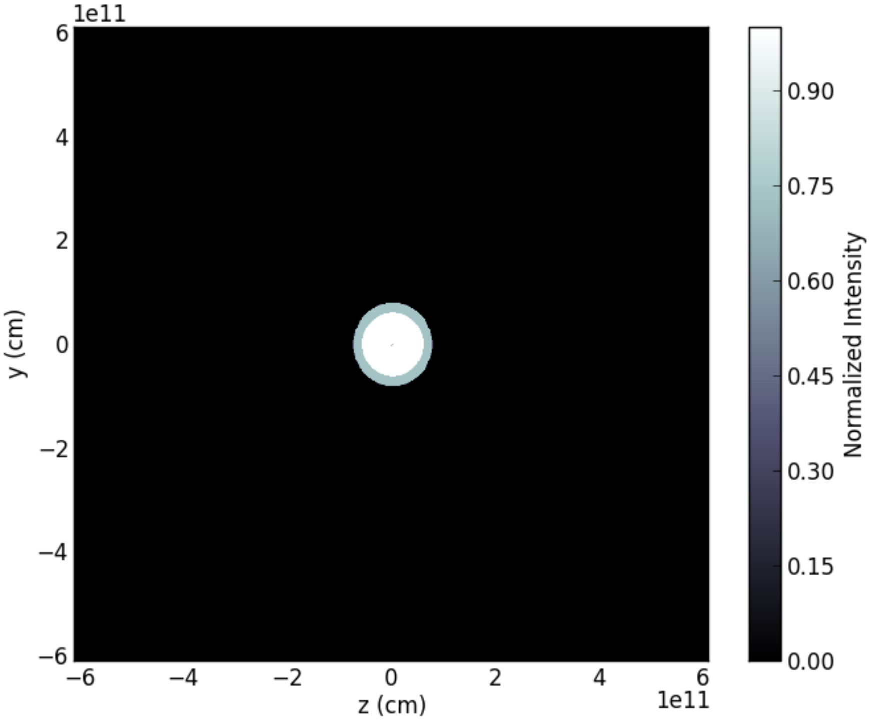

Figure 3.23: A mid-eclipse view of the 0.7 and 1.1 $M_\odot$ contact binary. The eclipse looks very similar to that shown in 3.21, but with the temperatures reversed, as it is the smaller star which in hotter in the contact system.

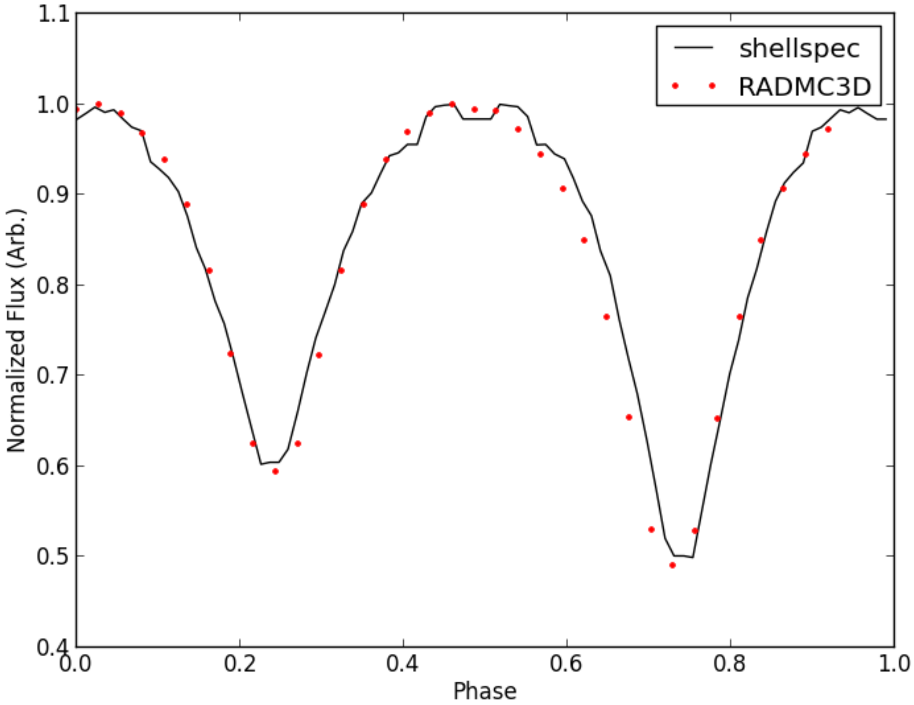

Figure 3.24: The light curve of the contact binary, with the `shellspec` curve in black and the `radmc3d` calculation in red. The expected broad eclipses are clearly evident, and with components of approximately the same surface temperature, the depths are approximately equal. The second eclipse is deeper, as expected.

Chapter 4

Conclusions

The previous chapters outline a method by which hydrodynamic simulations of stellar systems can be imaged, in a manner analogous to the formation of a real image on a CCD chip. `radmc3d` is a piece of software which solves the radiative transfer equation for an arbitrary user-defined geometry, with an comprised of astrophysical gas or dust, with an arbitrary set of user-selected spectral lines and user-defined continuous opacities.

We have shown that, given a model of a stellar atmosphere, *e.g.*, MARCS, we can accurately reproduce the black body spectrum of a star from a stellar model to a better than 0.1%. In order to test this, we first verified that the method behaved as expected analytically under the transition from optically-thin to optically-thick, using a sphere of uniform density and temperature with a varying opacity, with excellent agreement between the analytical prediction and the numerical result. Real stars presented and additional challenge, as the surface temperatures of the hydrodynamic models differed by two orders of magnitude from the expected effective temperature from YREC stellar evolution models. In order to properly calculate fluxes, a proper surface temperature was required. To calculate this temperature, an algorithm using the equation of hydrostatic equilibrium in the constant mass case was developed and used to integrate density and pressure outward. The integrated profile to density and pressure is used to interpolate in the (T,log(g)) space of the MARCS atmospheres, using the local log(g) and interpolated pressure and density to minimize the relative error in

$$\delta = \frac{|P_{\mathrm{SPH}} - P_{\mathrm{int}}|}{P_{\mathrm{SPH}}} + \frac{|\rho_{\mathrm{SPH}} - \rho_{\mathrm{int}}|}{\rho_{\mathrm{SPH}}} + \frac{|log(g)_{\mathrm{SPH}} - log(g)_{\mathrm{int}}|}{log(g)_{\mathrm{SPH}}}. \tag{4.1}$$

Interpolated temperatures were accurate to within ∼25%. Given the fact that each radmc3d grid cell is extremely optically thick, this temperature was assigned to the outermost two cells. Optically thick cells act as a hard boundary to photons attempting to travel through them, and so in this way the model mimics the true photosphere of a star, where the star becomes optically thick and all photons escape.

Black body spectra of stars were accurate to within less than 1% . Further photometry, namely light curves of detached and contact binaries are also reproduced with equal accuracy when compared to theoretical expectations from `shellspec` calculations. Predicting the surface temperature of contact binaries is difficult, as they are non-spherical. Care must be taken in deciding which grid cells are assigned to which star, for which we used a plane through the center of mass, perpendicular to the orbital plane. For an evolving orbit, this may not be the best criterion. A poor decision in "which cells belong to which object" can lead to a large error in surface gravity, which is an integral part of the error calculation. One option could be to use the local surface gravity, as determined by the hydrodynamic simulation, but the set up of `radmc3d` requires the a set of density and temperature files for each opacity, and a spatially varying surface gravity implies a spatially varying opacity, which increases the number of input files greatly.

The actual merger event will likely be beyond the scope of this method. The complete lack of symmetry will make the determination of even an approximate temperature very difficult. Here the only possible option would be to do each cell, individually, though a difficulty would still arise in determining a radius for the atmosphere integration. Considerable care must be taken in highly asymmetric situations such as this, and the choice of method will likely have to be motivated by the evolution of the merger itself.

4.1 Future Work

An obvious first step for future work on this project would be to to run an SPH simulation of a contact binary which leads to a merger and then apply this method to it to determine a synthetic light curve with can either be compared to the light curve shown in Figure 1 or used to set a lower limit on alternative theories, such as the one presented by Pejcha (2013), where instead of a merger and subsequent outburst, the sharp increase in the light curve was due instead to dynamical mass loss. This dynamical mass loss launches a wind which eventually becomes optically thick and obscures the binary. However, while the merger simulations are running and exploring the parameter space of possible progenitors, given by Stepien (2011), there is some additional work which could benefit the project greatly. Recent work by Nandez et al. (2013) extends on this and narrows the progenitor space greatly. Verification of the Nandez et al. (2013) results with photometry would be an excellent next step.

These merger events present a class of outbursts, called LNR, including objects such as V838 Monocerotis (Kimeswenger et al., 2002), M85 OT2006-1 (Rau et al., 2007) and M31 RV (Boschi & Munari, 2004). This method, when applied in generality, can be a valuable tool in understanding the evolution of these systems, and in working to understand the evolution of common envelope events.

There are a number of areas of this method which could be refined to gain higher accuracy or efficiency. The results presented in this chapter have all used cubic boxes with cubic grid cells, and in the case of the binary stars, there are a large proportion of grid cells which are out of the plane of the orbit, and are permanently zero valued in density and temperature. A more careful choice in box size and shape could cut the number of vertical pixels by half, which would considerably reduce memory use, especially considering that nothing whatsoever is happening in these cells. In the case of a merger, this may not be the case for the entire lifetime of the merger event depending if mergers form an excretion disk or an excretion shell, but is at least a plausible option for optimization. Additionally, `radmc3d` has, built in, the capacity to deal with adaptive grids. Grid codes with adaptive grids to refine the size of cells in areas of high density, to pick up on finer structure without globally refining the grid in a way that inflates memory usage without gaining further accuracy. In the case of stellar systems, and in particular stellar mergers, it is not the high density regions, but the low density regions which are of particular interest. If SPLASH could be modified to convert from SPH onto a refined grid based on a refinement criteria, the majority of the star, where very little of interest occurs, could be contained in one or a few cells large cells, with a large number of highly-refined cells making up the atmosphere. This could improve efficiency of the imaging process and accuracy of the interpolation process, with individual cells coming much closer to the actually thickness of the atmosphere.

Bibliography

Abazajian, K. N., Adelman-McCarthy, J. K., Agüeros, M. A., Allam, S. S., Allende Prieto, C., An, D., Anderson, K. S. J., Anderson, S. F., Annis, J., Bahcall, N. A., & et al. 2009, The Astrophysical Journal Supplement, 182, 543

Adelman, S. J. 2004, in IAU Symposium, Vol. 224, The A-Star Puzzle, ed. J. Zverko, J. Ziznovsky, S. J. Adelman, & W. W. Weiss, 1–11

Bate, M. 1995, PhD thesis, Univ. Cambridge, (1995)

Boschi, F. & Munari, U. 2004, Astronomy and Astrophysics, 418, 869

Boss, A. P. 2008, The Astrophysical Journal, 677, 607

Budaj, J. & Richards, M. T. 2004, Contributions of the Astronomical Observatory Skalnate Pleso, 34, 167

Carroll, B. W. & Ostlie, D. A. 2006, An Introduction to Modern Astrophysics and Cosmology (San Francisco, California: Pearson)

Demarque, P., Guenther, D. B., Li, L. H., Mazumdar, A., & Straka, C. W. 2007, Astrophysics and Space Science, 316, 31

Dullemond, C. P. 2012, RADMC-3D: A multi-purpose radiative transfer tool, astrophysics Source Code Library

Duquennoy, A. & Mayor, M. 1991, A&A, 248, 485

Forgan, D. & Rice, K. 2010, Monthly Notices of the Royal Astronomical Society, 406, 10

Gazeas, K. & Stepien, K. 2008, Monthly Notices of the Royal Astronomical Society, 390, 1577

Gilliland, R. L., Brown, T. M., Christensen-Dalsgaard, J., Kjeldsen, H., Aerts, C., Appourchaux, T., Basu, S., Bedding, T. R., Chaplin, W. J., Cunha, M. S., De Cat, P., De Ridder, J., Guzik, J. A., Handler, G., Kawaler, S., Kiss, L., Kolenberg, K., Kurtz, D. W., Metcalfe, T. S., Monteiro, M. J. P. F. G., Szabó, R., Arentoft, T., Balona, L., Debosscher, J., Elsworth, Y. P., Quirion, P.-O., Stello, D., Suárez, J. C., Borucki, W. J., Jenkins, J. M., Koch, D., Kondo, Y., Latham, D. W., Rowe, J. F., & Steffen, J. H. 2010, Publications of the Astronomical Society of the Pacific, 122, 131

Gingold, R. A. & Monaghan, J. J. 1977, Monthly Notices of the Royal Astronomical Society, 181, 375

Gustafsson, B., Edvardsson, B., Eriksson, K., Jørgensen, U. G., Nordlund, Å., & Plez, B. 2008, A&A, 486, 951

Kimeswenger, S., Lederle, C., Schmeja, S., & Armsdorfer, B. 2002, Monthly Notices of the Royal Astronomical Society, 336, L43

Kopal, Z. 1959, The International Astrophysics Series: Close Binary Systems (London: Chapman & Hall)

Kurucz, R. L. 1995, Astrophysical Applications of Powerful New Databases. Joint Discussion No. 16 of the 22nd. General Assembly of the I.A.U., 78

Lajoie, C.-P. & Sills, A. 2010, The Astrophysical Journal, 726, 10

Lucy, L. B. 1977, The Astronomical Journal, 82, 1013

Nakano, S., Nishiyama, K., Kabashima, F., Sakurai, Y., Jacques, C., Pimentel, E., Chekhovich, D., Korotkiy, S., Kryachko, T., & Samus, N. N. 2008, V1309 Scorpii = Nova Scorpii 2008

Nandez, J. L. A., Ivanova, N., & Lombardi, Jr, J. 2013, ArXiv preprint astro-ph/1311.6522

Nicholls, C. P., Melis, C., Soszynski, I., Udalski, A., Szymanski, M. K., Kubiak, M., Pietrzynski, G., Poleski, R., Ulaczyk, K., Wyrzykowski, L., Kozlowski, S., & Pietrukowicz, P. 2013, Monthly Notices of the Royal Astronomical Society: Letters

Pejcha, O. 2013, ArXiv preprint astro-ph/1307.4088

Peraiah, A. 2002, An Introduction to Radiative Transfer: Methods and applications in astrophysics (Cambridge Univ Pr)

Peytremann, E. 1974, Astronomy and Astrophysics, 33, 203

Price, D. J. 2012, Journal of Computational Physics, 231, 759

—. 2013, Publications of the Astronomical Society of Australia, 24, 159

Raghavan, D., McAlister, H. A., Henry, T. J., Latham, D. W., Marcy, G. W., Mason, B. D., Gies, D. R., White, R. J., & ten Brummelaar, T. A. 2010, The Astrophysical Journal Supplement Series, 190, 1

Rau, A., Kulkarni, S. R., Ofek, E. O., & Yan, L. 2007, The Astrophysical Journal, 659, 1536

Riess, A. G., Filippenko, A. V., Challis, P., Clocchiatti, A., Diercks, A., Garnavich, P. M., Gilliland, R. L., Hogan, C. J., Jha, S., Kirshner, R. P., Leibundgut, B., Phillips, M. M., Reiss, D., Schmidt, B. P., Schommer, R. A., Smith, R. C., Spyromilio, J., Stubbs, C., Suntzeff, N. B., & Tonry, J. 1998, The Astronomical Journal, 116, 1009

Robitaille, T. P. 2011, Astronomy & Astrophysics, 536, A79

Rybicki, G. B. & Lightman, A. P. 1986, Radiative Processes in Astrophysics (Wiley)

Seaton, M. J., Yan, Y., Mihalas, D., & Pradhan, A. K. 1994, Monthly Notices of the Royal Astronomical Society, 266, 805

Sneden, C., Johnson, H. R., & Krupp, B. M. 1976, The Astrophysical Journal, 204, 281

Spergel, D. N., Verde, L., Peiris, H. V., Komatsu, E., Nolta, M. R., Bennett, C. L., Halpern, M., Hinshaw, G., Jarosik, N., Kogut, A., Limon, M., Meyer, S. S., Page, L., Tucker, G. S., Weiland, J. L., Wollack, E., & Wright, E. L. 2003, The Astrophysical Journal Supplement Series, 148, 175

Springel, V. 2010, Annual Review of Astronomy and Astrophysics, 48, 391

Stamatellos, D. & Whitworth, A. 2005, Arxiv preprint astro-ph/0505289, 2951

Stepien, K. 2011, Astronomy & Astrophysics, 531, 5

Tylenda, R., Hajduk, M., Kamiski, T., Udalski, A., Soszyski, I., Szymaski, M. K., Kubiak, M., Pietrzyski, G., Poleski, R., Wyrzykowski, L., & Ulaczyk, K. 2010, Astronomy & Astrophysics, 528, 1

Webbink, R. F. 2003, in Astronomical Society of the Pacific Conference Series, Vol. 293, 3D Stellar Evolution, ed. S. Turcotte, S. C. Keller, & R. M. Cavallo, 76

Ziegel, E., Press, W., Flannery, B., Teukolsky, S., & Vetterling, W. 1987, Technometrics, 29, 501